

1 *This manuscript has been accepted for publication in the journal Chemical Geology*
2

3 **Improving the reliability of Fe- and S-XANES measurements in silicate glasses:**
4 **correcting beam damage and identifying Fe-oxide nanolites in hydrous and**
5 **anhydrous melt inclusions**

6
7 Allan H. Lerner^{1*}, Michelle J. Muth¹, Paul J. Wallace¹, Antonio Lanzirotti², Matthew Newville²,
8 Glenn A. Gaetani³, Proteek Chowdhury⁴, Rajdeep Dasgupta⁵
9

10 ¹ Department of Earth Sciences, University of Oregon, Oregon 97403, USA

11 ² Center for Advanced Radiation Sources, The University of Chicago, Illinois 60637, USA

12 ³ Department of Geology and Geophysics, Woods Hole Oceanographic Institution, Woods Hole,
13 Massachusetts 02543, USA

14 ⁴ Department of Earth and Planetary Sciences, University of California, Riverside, CA 92521, USA

15 ⁵ Department of Earth, Environmental, and Planetary Sciences, Rice University, Texas 77005, USA

16 * Corresponding author at: 1272 University of Oregon, Eugene, OR 97403, USA. *E-mail address:*
17 lerner.allan@gmail.com (A. H. Lerner).
18

19 **Highlights**

- 20 • Photo-oxidation during Fe-XANES analyses of glasses can be corrected by time-
21 dependent restorations to initial values
22 • Photo-reduction can occur rapidly during S-XANES analyses even in glasses that are
23 stable during Fe-XANES analysis
24 • Photo-reduction during S-XANES can be corrected by restoring S⁴⁺ to S⁶⁺ signal
25 intensities
26 • Fe-oxide nanolites in otherwise glassy melt inclusions can be identified by magnetite-like
27 features in Fe-XANES spectra
28 • Beam damage correction techniques enable accurate XANES measurements of damage-
29 susceptible glasses and melt inclusions

30 Abstract

31 The redox state of silicate melts influences crystallization, element partitioning, and
32 degassing behavior. Synchrotron-based micro-X-ray absorption near edge structure (μ XANES)
33 spectroscopy has emerged as a powerful tool for determining redox conditions through the direct
34 measurement of speciation of multivalent elements such as iron and sulfur in silicate glasses. In
35 particular, the high spatial resolution afforded by synchrotron μ XANES makes it one of the few
36 techniques available for determining redox conditions in melt inclusions, which can provide
37 insights into pre-eruptive melt properties. However, the small size of melt inclusions, the deep
38 penetration of X-rays, and irradiation-induced beam damage make μ XANES measurements in
39 melt inclusions challenging. Here we present data that show rapid Fe- and S- μ XANES beam
40 damage in experimental glasses, mid-ocean ridge basalt glasses, and olivine-hosted melt
41 inclusions from the southern Cascade arc and Kīlauea Volcano and develop approaches to
42 recognize and correct for beam damage through repeated rapid analyses. By applying a time-
43 dependent correction to a series of rapid measurements (~ 82 s/scan) of Fe- μ XANES pre-edge
44 centroid positions, irradiation-induced photo-oxidation (Fe^{2+} to Fe^{3+}) can be corrected back to
45 undamaged initial $\text{Fe}^{3+}/\Sigma\text{Fe}$ even in damage-susceptible hydrous glasses. Using this beam
46 damage correction technique, hydrous basaltic melt inclusions from the southern Cascades have
47 $\text{Fe}^{3+}/\Sigma\text{Fe}$ that is ~ 0.036 lower (corresponding to -0.5 log units lower oxygen fugacity) than would
48 have been indicated by standard Fe- μ XANES measurements. Repeated, rapid analyses (150 –
49 300 s/scan) were used to identify S- μ XANES beam damage (photo-reduction of S^{6+} to S^{4+}),
50 which was corrected with a peak fitting method to restore initial $\text{S}^{6+}/\Sigma\text{S}$. We observe that S-
51 μ XANES beam damage can occur rapidly even in low- H_2O mid-ocean ridge basaltic glasses and
52 melt inclusions from Kīlauea Volcano, which are otherwise stable during even prolonged Fe-
53 μ XANES analyses. By mitigating and correcting for sulfur photo-reduction, we conclude that
54 some mid-ocean ridge basaltic glasses contain $0.08 - 0.09$ $\text{S}^{6+}/\Sigma\text{S}$, which is more sulfate than
55 might be expected based on the reduced oxidation state of these glasses (near the fayalite-
56 magnetite-quartz oxygen buffer). Using beam damage identification and correction techniques,
57 the valence states of iron and sulfur can be accurately measured even in beam damage-
58 susceptible glasses and melt inclusions. Finally, using Fe- μ XANES, we demonstrate the
59 presence of Fe-oxide nanolites within otherwise glassy, naturally quenched melt inclusions,
60 which can complicate determination of iron valence state in affected glasses.

61

62 **Key words:** XANES; Beam Damage; Nanolites; Sulfur; Iron; Melt Inclusions

63

64 **1.1 Introduction**

65 Synchrotron-based micro-X-ray absorption near edge structure (μ XANES) spectroscopy
66 has become a valuable petrologic tool for *in situ* determination of the valence state and molecular
67 complexing of redox-sensitive elements in magmatic minerals and glasses (see review by Sutton
68 et al., 2020). In particular, Fe- and S- μ XANES have been applied to quenched volcanic glasses
69 to advance our understanding of magmatic oxygen fugacity (fO_2) and complexing of species in
70 glasses from Earth's mid-ocean ridges, hotspots, and volcanic arcs (Bonnin-Mosbah et al., 2001,
71 2002; Wilke et al., 2006; Berry et al., 2008; Kelley and Cottrell, 2009; Cottrell and Kelley, 2011;
72 Brounce et al., 2014, 2017; Dyar et al., 2016; Lanzirotti et al., 2019; Moussallam et al., 2019;
73 Sutton et al., 2020), as well as in igneous material from lunar and Martian samples (Righter et
74 al., 2013; McCanta et al., 2017, 2019). The fO_2 of magmas exerts a major control on mineral
75 stability and thereby the differentiation paths of magmas (Osborn, 1959; Kelley and Cottrell,
76 2012), including the behavior of important ore-forming species (e.g. Cr, Cu, Fe, Ti; Papike et al.,
77 2016; Lanzirotti et al., 2019; Sutton et al., 2020). Additionally, fO_2 can significantly affect the
78 solubility and degassing of multivalent volatiles (e.g., S, C) (Jugo, 2009; Jugo et al., 2010; de
79 Moor et al., 2013; Jégo and Dasgupta, 2014; Moussallam et al., 2014, 2016; Helz et al., 2017;
80 Head et al., 2018). A well-established approach to determining melt fO_2 is by measuring
81 $Fe^{3+}/\Sigma Fe$ in quenched glasses (e.g., Kress and Carmichael, 1991; Borisov et al., 2018; O'Neill et
82 al., 2018).

83 Iron occurs as both Fe^{2+} and Fe^{3+} in most terrestrial melts, and as Fe^{2+} or Fe^0 in strongly
84 reduced melts below the IW buffer (generally extraterrestrial) (Schreiber et al., 1987). Fe-
85 XANES allows the mean valence state of iron in minerals and silicate glasses to be determined
86 based on spectral features at energies below the iron absorption edge (pre-edge features), while
87 higher energy features inform iron bonding coordination in minerals (e.g., Waychunas et al.,
88 1983; Bajt et al., 1994; Wilke et al., 2001, 2004, 2006; Berry et al., 2003, 2008; Farges et al.,
89 2004; Cottrell et al., 2009). Fe-XANES pre-edge features in glasses are specifically sensitive to
90 valence state, and measured spectra can therefore be related to glass $Fe^{3+}/\Sigma Fe$ by comparison to

91 suites of glass standards synthesized under controlled redox conditions and analyzed using
92 Mössbauer spectroscopy (e.g., Berry et al., 2003; Wilke et al., 2004; Cottrell et al., 2009).
93 Several published calibrations relate measured Fe-XANES spectral centroid position associated
94 with Fe²⁺ and Fe³⁺ pre-edge peaks to Fe³⁺/ΣFe in silicate glasses (Galoisy et al., 2001; Bonnin-
95 Mosbah et al., 2001; Berry et al., 2003; Wilke et al., 2004, 2007; Cottrell et al., 2009; Dauphas et
96 al., 2014; Zhang et al., 2016, 2018; Fiege et al., 2017). Other recent calibrations have used
97 multivariate analysis of the entire Fe-XANES spectrum to determine iron valence in standard
98 glasses measured by Mössbauer (Shorttle et al., 2015; Dyar et al., 2016).

99 Sulfur in silicate melts dominantly occurs as S²⁻ or S⁶⁺ (Carroll and Rutherford, 1988;
100 Wilke et al., 2008). The transition between S²⁻ and S⁶⁺ species in silicate melts occurs over a
101 relatively narrow *f*O₂ range near the Ni-NiO buffer (Carroll and Rutherford, 1988; Jugo et al.,
102 2010; Botcharnikov et al., 2011), although there is evidence that this transition is dependent on
103 pressure, temperature, and melt composition (Baker and Moretti, 2011; Klimm et al., 2012a;
104 Fiege et al., 2014; Masotta and Keppler, 2015; Matjuschkin et al., 2016; Nash et al., 2019). S-
105 XANES has been used to quantify the S⁶⁺/ΣS in glasses by fitting the relative intensity of
106 absorption peaks for sulfide and sulfate species that occur at ~2475 – 2479 and ~2481 – 2483
107 eV, respectively (Paris et al., 2001; Métrich et al., 2002, 2009; Bonnin-Mosbah et al., 2002; Fleet
108 et al., 2005; Jugo et al., 2010). These two sulfur species generally have distinct spectral
109 absorbance features when present in silicate glasses. Based on melt composition and cooling
110 history, reduced sulfur can also occur in a variety of metal-sulfide complexes, each of which has
111 particular identifiable spectroscopic features (Li et al., 1995; Bonnin-Mosbah et al., 2002; Fleet
112 et al., 2005; Head et al., 2018).

113 Fe- and S-XANES are particularly powerful techniques for investigating redox conditions
114 of melt inclusions (MI), which are small parcels of quenched glass formed from melt entrapped
115 within growing crystals. Melt inclusions are useful because they can preserve information on
116 volatile concentrations and melt diversity that is otherwise lost during magma mixing, ascent,
117 and eruption (Kent, 2008; Métrich and Wallace, 2008; Wallace et al., 2021). Melt inclusions in
118 many systems of petrologic interest have mean diameters of 10 – 100 μm. The small size of MI
119 leaves μXANES (hereafter XANES) as one of the few techniques suitable for *in situ*
120 measurements of element speciation (i.e., valence state and molecular coordination) within MI.

121 Of course, inferring magma redox state from iron and sulfur valence in quenched glasses
122 requires accurate XANES measurements. The large penetrative depths of high-energy X-rays
123 and oblique incident beam trajectories at many analytical facilities require careful sample
124 preparation and analytical strategies to avoid signal contamination during Fe- and S-XANES
125 measurements of MI and matrix glasses (Figure 1). It has also been recognized that many glass
126 compositions are susceptible to X-ray induced changes in iron and sulfur speciation during
127 analysis (i.e., beam damage) (Wilke et al., 2008; Métrich et al., 2009; Gonçalves Ferreira et al.,
128 2013; Moussallam et al., 2014, 2019; Cottrell et al., 2018; Hughes et al., 2020). Although Fe-
129 XANES measurements of nominally anhydrous basaltic and rhyolitic glasses are observed to be
130 reproducible over a broad range of incident X-ray fluxes (Cottrell et al., 2009), hydrous volcanic
131 glasses, particularly basaltic compositions, have been observed to undergo rapid oxidation of
132 Fe²⁺ to Fe³⁺ with progressive irradiation (Cottrell et al., 2018; Moussallam et al., 2019). The
133 exact mechanisms of iron photo-oxidation are not fully understood, but involve the production of
134 photoelectrons and the local accumulation of charge in non-conductive materials, which alters
135 the electron state of multivalent elements. The ensuing redox exchanges within glasses are
136 accelerated by O-H volatilization or migration (Cottrell et al., 2018).

137 S-XANES measurements in silicate glasses have also been observed to undergo beam-
138 induced changes in speciation, typically with S⁶⁺ being reduced to S⁴⁺ during progressive X-ray
139 irradiation (Wilke et al., 2008; Métrich et al., 2009). Strategies to mitigate beam damage during
140 Fe- and S-XANES measurements include reducing X-ray flux density (photon flux/analytical
141 area) by using defocused beams, continually moving the sample during analysis, and/or
142 decreasing incident photon flux (Wilke et al., 2008; Métrich et al., 2009; Klimm et al., 2012a;
143 Brounce et al., 2017; Cottrell et al., 2018; Moussallam et al., 2019). Spatially resolved XANES
144 beamlines are available at a number of synchrotron light sources worldwide with incident X-ray
145 intensities ranging from 10⁸ – 10¹² photons/s (Sutton et al., 2020), where higher X-ray fluxes
146 shorten analysis time by providing lower detection limits, but amplify beam damage concerns.

147 Many of these approaches to lessen beam damage are challenging to apply to MI owing
148 to their small sizes. Smaller MI require more focused beam diameters to avoid contamination by
149 the host-phase, but are thereby subject to higher photon densities and thus possible beam damage
150 (e.g., Gaborieau et al., 2020; Tassara et al., 2020). Melt inclusions are often targeted for
151 petrological investigation specifically because they can retain magmatic volatiles that are

152 otherwise lost from the external magma during ascent and degassing (Kent, 2008; Métrich and
153 Wallace, 2008). However, silicate glasses with high H₂O content have been observed to undergo
154 larger changes in iron (and potentially sulfur) speciation during irradiation than what is observed
155 in anhydrous silicate glasses (Cottrell et al., 2018; Moussallam et al., 2019). Hydrous MI may
156 also be susceptible to the formation of nanolite crystals during quenching (Danyushevsky et al.,
157 2002; Di Genova et al., 2018), which may lead to spurious interpretation of XANES spectra.
158 These combined properties make it particularly challenging to apply XANES oxybarometry
159 methods to the analysis of MI from volcanic arc environments, which tend to be both small and
160 H₂O-rich.

161 For these more challenging MI, it is beneficial to develop XANES approaches that both
162 minimize changes in elemental speciation during irradiation and correct for changes that do
163 occur. Applying generalized corrections to datasets is not ideal because differences in glass
164 compositions and H₂O contents (e.g., caused by variable diffusive H⁺ loss from MI before
165 quenching) can lead to different MI susceptibilities to beam damage within the same deposit or
166 even within the same host mineral.

167 In this study, we present techniques that aid in recognizing X-ray--induced changes in
168 iron and sulfur valence in volcanic glasses and MI that result from XANES analysis. We then
169 propose new time-dependent corrections for beam damage that does occur. For S-XANES, we
170 also introduce a new spectral fitting approach that may better account for reduction of S⁶⁺ to S⁴⁺
171 during analysis. Finally, we present a method to identify the presence of Fe-oxide nanolites in
172 MI during Fe-XANES analysis. Collectively, these methods enable reliable quantification of iron
173 and sulfur valence, and thereby melt redox state, from small and/or beam damage-susceptible
174 glasses and MI.

175

176 **2.1 XANES analysis of melt inclusions**

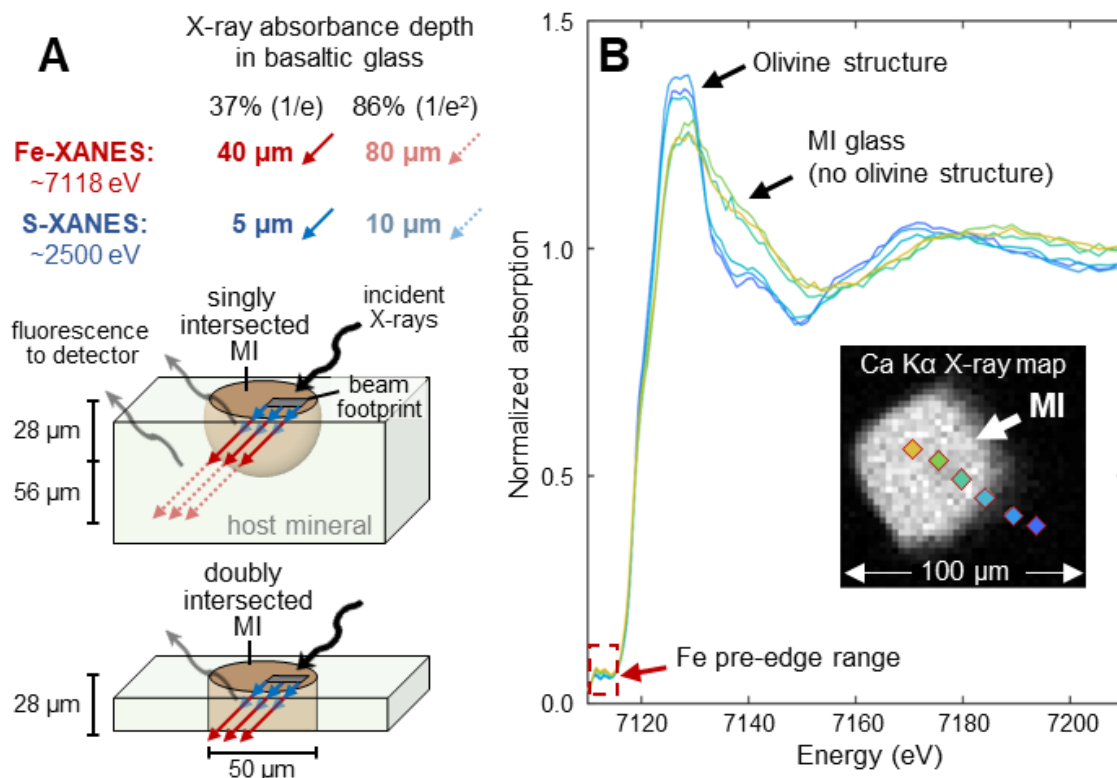
177 **2.1.1 Geometric considerations**

178 At the Fe *K*-edge, the characteristic 1/e X-ray absorption depth in basaltic glass is ≈ 40
179 μm (Elam et al., 2002), and 120 μm (1/e³) thick glass is therefore required for 95% absorption of
180 X-rays during Fe-XANES measurements. X-ray absorption by Fe-bearing inclusions or
181 crystalline host phases that may be present within the analytical path will be mixed with the

182 signal of the targeted glass. This is a particular problem for analyzing MI, as MI are often less
183 than 100 μm thick. Consequently, most MI must be doubly intersected for Fe-XANES analysis
184 to avoid signal contamination from the host mineral. A further complication in XANES
185 measurements of MI, particularly for highly penetrative Fe-XANES analyses, is that many
186 μXANES beamline configurations utilize a $\sim 45^\circ$ slant geometry of incoming X-ray beam in
187 fluorescence operating modes. The inclined incidence angle means that as wafer thickness
188 increases in the beam direction, progressively wider doubly-intersected MI areas are needed to
189 keep the analytical path free of mineral contamination (Figure 1). Throughout the X-ray
190 penetration volume, the minimum required doubly-intersected MI dimensions for a host-free
191 glass measurement are roughly equal to MI thickness plus the beam diameter size (assuming a
192 cylindrical doubly-intersected MI area). This requires MI to be either sufficiently wide or ground
193 very thin for clean glass analyses using high energy X-rays (e.g., Fe-XANES, V-XANES, Cu-
194 XANES). Thus, small MI in olivine and other Fe-bearing phases can be challenging to measure
195 for Fe-XANES. Even for analyses of MI in phases that have low, but non-zero, Fe-
196 concentrations (e.g., feldspars), the high penetrative depth of Fe-XANES can excite a large
197 volume of the host phase, so that the host contribution to the Fe-XANES signal may be
198 significant. This issue is of particular concern for small MI and for glass compositions with
199 relatively low Fe-contents, such as dacites and rhyolites. At the lower energy S *K*-edge (~ 2500
200 eV), X-rays are more strongly attenuated, with the $1/e$ X-ray absorption depth in basaltic glass
201 only $\sim 5 \mu\text{m}$. Consequently, 95% of the S-XANES X-ray absorption occurs within the upper 15
202 μm and most of these geometric concerns are accordingly lessened (Figure 1A).

203

204



205

206 **Figure 1.** (A) Schematic analytical XANES geometry of a 50 μm diameter melt inclusion (MI)
 207 (brown) analyzed with a 20×20 μm X-ray beam. For many XANES fluorescence measurements,
 208 the X-ray beam (black arrow) is ~45° incident to the sample surface and the sample fluorescent
 209 energy (gray arrows) is measured at 45° in the opposite direction. Depending on the penetration
 210 depth of the X-ray energy being used, the beam may interact with substantial host mineral both
 211 laterally and at depth, leading to mineral-contaminated spectra. For Fe-XANES (red arrows),
 212 37% and 86% of the X-ray signal are absorbed in 40 and 80 μm hypotenuse paths through
 213 basaltic glass (28 and 56 μm vertical thicknesses), requiring the MI be both doubly intersected
 214 and sufficiently wide to avoid host mineral contamination. S-XANES X-ray energies are much
 215 less penetrating (blue arrows), so MI geometry and thickness concerns are lessened. (B) A series
 216 of Fe-XANES measurements of a doubly-intersected olivine-hosted MI from the southern
 217 Cascades (BORG-1_37, Table 1) showing a traverse from within the MI into the olivine-host,
 218 demonstrating the difference in absorption edge shape between analyses of glass and of olivine.
 219 Measurement locations are shown atop a Ca K α X-ray map (inset), with symbol colors matching
 220 the shown spectra.

221

222 2.1.2 Analytical details and sample descriptions

223 Fe- and S-XANES measurements were conducted on a variety of volcanic and
 224 experimental silicate glasses at GSECARS beamline 13-ID-E at Argonne National Laboratory's
 225 (Illinois, USA) Advanced Photon Source (APS), a third generation synchrotron light source
 226 (Sutton et al., 2017). Details of the 13-ID-E beamline configuration are described in Head et al.

227 (2018) and are consistent with measurements conducted here, except for differences in photon
228 flux and analytical times described below.

229 To account for differences in monochromator calibrations between synchrotron facilities,
230 a set of standards (minerals, metal foils, synthetic glasses) were measured at the onset of each
231 analytical session to determine the appropriate energy offset to apply to Fe- and S-XANES
232 oxybarometer calibration curves relative to reference energy fitting ranges (details below). At
233 beamline 13-ID-E, the lattice constants for the monochromator Si(111) and Si(311) crystals are
234 calculated from reference foils measured throughout the analyzable energy range of the crystals,
235 and provide excellent consistency with absorption edge energies determined by Kraft et al.
236 (1996). The 13-ID-E beamline has excellent reproducibility in measured reference materials over
237 the course of standard two to three-day measurement periods and therefore no within-session
238 drift corrections were applied during either Fe- or S-XANES measurements. Prior to each
239 XANES analysis, an X-ray map was made by rapidly rastering across the sample to identify
240 areas in MI and other glass targets that were free of host mineral and microlite crystals in the
241 beam path. The X-ray beam was then turned off to prevent any further unnecessary beam
242 interaction with the glasses until XANES measurements began.

243 Analyzed samples include doubly-intersected MI and matrix glasses mounted on Fe-free
244 glass rounds and thin sections. Samples were embedded in CrystalBond®, EpoThin® epoxy, or
245 thin section resin. All bonding material and glass substrates were analyzed to confirm that they
246 contained only trace iron and had negligible contribution to Fe-XANES signals. The bonding
247 materials did contain substantial S, but the low energy X-rays for S-XANES measurements are
248 fully absorbed within a ~20 μm path within basaltic glasses (15 μm vertical path with 45°
249 incident beam angle, Figure 1A). All analyzed MI and matrix glass areas are thicker than 20 μm ,
250 so that the bonding materials contributed no appreciable signal to S-XANES measurements. We
251 also analyzed singly intersected experimental glass charges, where glass thicknesses of multiple
252 mm fully absorbed X-rays at both Fe- and S- $K\alpha$ energies so that contamination from the capsule
253 material was insignificant. In experimental glass charges, care was taken to analyze only crystal-
254 poor glass areas and to avoid measurements near capsule edges.

255
256
257

258 **Table 1:** Experimental and natural glasses analyzed by Fe- and S-XANES in this study.

Sample, composition	H ₂ O (wt%)	Fe-XANES beam damage susceptibility index (Φ)*	XANES analysis type	Fe ³⁺ /ΣFe and S ⁶⁺ /ΣS ranges**	Photon density (photons/s/μm ²); observed beam damage***
CAB-47: experimental basaltic glass. 1250 °C, 1.3 GPa, minor phenocrysts (Weaver et al., 2011; this study)	5.5	1.6	Fe-XANES (+ photo-oxidation time series tests) S concentration too low for S-XANES	0.13 Fe ³⁺	Fe-XANES: 1 – 1.5×10 ⁸ : high 2 – 4×10 ⁷ : high 6 – 9×10 ⁶ : med
CAB-33: experimental basaltic glass. 1225 °C, 1.7 GPa, phenocryst-free, but Fe-oxide nanolite spectral signature (Weaver et al., 2011; this study)	7.2	1.8	Fe-XANES (+ photo-oxidation time series tests) S concentration too low for S-XANES	Fe-oxide nanolites present	Fe-XANES: 2 – 4×10 ⁷ : severe 6 – 9×10 ⁶ : high
P2-F: Mono Craters obsidian pyroclast with <0.1% microlites (Barnes et al., 2014; Watkins et al., 2017; this study)	2.0 – 2.3	-	Fe photo-oxidation time series tests	-	Fe-XANES: 1 – 1.5×10 ⁸ : med 2 – 4×10 ⁷ : slight
G466: experimental basalt glass. 1300 °C, 2 GPa, minor clinopyroxene + anhydrite (Chowdhury and Dasgupta, 2019; this study)	6.5	-	S-XANES	1.0 S ⁶⁺	S-XANES: 5×10 ⁹ : severe 2×10 ⁸ : high 5×10 ⁷ : med 8×10 ⁶ : slight
G479: experimental basalt glass. 1300 °C, 1.5 GPa, minor anhydrite (Chowdhury and Dasgupta, 2019; this study)	8.9	-	S-XANES	1.0 S ⁶⁺	S-XANES: 8×10 ⁶ : slight
MORB glasses: VG-2 (Jarosewich et al., 1980; Rose and Brown, 2017; Zhang et al., 2018; this study) JDF-46N (Fiege et al., 2014; this study) ALV892-1 (Fiege et al., 2014; this study)	<0.1	~0.01	S-XANES	~0.15 Fe ³⁺ 0.04 – 0.08 S ⁶⁺	S-XANES: 1×10 ¹⁰ : severe 4.5×10 ⁸ : high 1×10 ⁸ : med 6.5×10 ⁶ : slight
KE62-3293S: Kīlauea 2018 basaltic pumice MI and matrix glass (Lerner et al., in revision; this study)	0.1 – 0.3	0.1	Fe-XANES S-XANES	0.13 – 0.18 Fe ³⁺ 0.03 – 0.25 S ⁶⁺	Fe-XANES: 2 – 4×10 ⁷ : none S-XANES: 2×10 ⁸ : med 5×10 ⁷ : slight 8×10 ⁶ : none
KE62-3315F: Kīlauea 2018 littoral bomb MI and matrix glass (Lerner et al., in revision; this study)	0.1 – 0.2	0.03	Fe-XANES S-XANES	0.20 – 0.34 Fe ³⁺ 0.68 – 0.96 S ⁶⁺	Fe-XANES: 2 – 4×10 ⁷ : none S-XANES: 5×10 ⁷ : high 8×10 ⁶ : slight
Lassen (southern Cascades): olivine-hosted MI BRM, BBL, BORG (Muth and Wallace, 2021; this study)	0.3 – 3.7	0.1 – 0.7	Fe-XANES S-XANES	0.14 – 0.31 Fe ³⁺ 0.20 – 0.98 S ⁶⁺	Fe-XANES: 2 – 4×10 ⁷ : med S-XANES: 5×10 ⁷ : med 8×10 ⁶ : slight
Augustine 2006: AUG_308 – low silica andesite tephra; AUG_HSA2 – high silica andesite tephra (Lerner, 2020; this study)	1.0 – 4.0	0.2	Fe-XANES	0.39 – 0.44 Fe ³⁺ (in glasses with no Fe-oxide nanolites)	Fe-XANES: 1 – 1.5×10 ⁸ : slight to none
Cerro Negro: olivine-hosted MI (Gaetani et al., 2012; this study)	3.0 – 4.0	0.5	Fe-XANES	Fe-oxide nanolites present	Fe-XANES: not tracked with repeat scans

* Fe-XANES beam damage susceptibility index (Cottrell et al., 2018): $XH_2O \cdot 2XFeO / XFe_2O_3$, calculated using molar fractions and Fe^{2+}/Fe^{3+} from time-zero interpolated Fe-XANES measurements. Full glass compositions are presented in the **Data supplement**.

** $Fe^{3+}/\Sigma Fe$ and $S^{6+}/\Sigma S$ ranges for beam damage corrected Fe- and S-XANES analyses. XANES spectra and results are presented in the **Data supplement**.

*** Incident photon flux was $\sim 3 - 5 \times 10^9$ photons/s for Fe-XANES, and $\sim 1 - 50 \times 10^9$ photons/s for S-XANES. Analysis footprint sizes ranged from 2×2 , 5×5 , 10×10 , 20×20 , and 50×50 μm . Qualitative beam damage observations were based on 2 – 4 repeated scans, with total scan times of 8 – 12 minutes and 10 – 15 minutes per location for Fe- and S-XANES measurements, respectively.

259

260 2.2 Identifying and correcting Fe-XANES beam damage

261 Fe-XANES measurements were made in fluorescence mode at APS during analysis
262 sessions in 2018 and 2019. The APS 13-ID-E beamline can deliver a focused, unattenuated X-
263 ray beam to the sample at the Fe *K*-edge energy with a photon flux exceeding 1×10^{12} photons/s.
264 Fully focused beam sizes of $\sim 1 \times 2$ μm are achievable, providing flux densities up to 5×10^{11}
265 photons/s/ μm^2 . Cottrell et al. (2018) and Moussallam et al. (2019) show that beam damage
266 during Fe-XANES analysis scales with delivered photon dose over the measurement duration.
267 Therefore, for the analyses presented here, photon dose was minimized during Fe-XANES
268 analyses as follows:

- 269 1) Photon flux was attenuated using high-purity aluminum foil filters in the beam path (6
270 sheets of foil, totaling 222 μm thick), which decreased the incident photon flux to $\sim 3 -$
271 5×10^9 photons/s, consistent with an approach used in previous studies (Brounce et al.,
272 2017; Moussallam et al., 2019; Tassara et al., 2020; Gaborieau et al., 2020).
- 273 2) Flux density on the sample was further decreased by defocusing the incident X-ray beam
274 so that photon densities were generally $1 - 1.5 \times 10^8$, $2 - 4 \times 10^7$, and $6 - 9 \times 10^6$
275 photons/s/ μm^2 for 5×5 , 10×10 , and 20×20 μm beam footprints, respectively.
- 276 3) Analysis times were minimized as much as possible while still providing interpretable
277 spectra, which allowed us to reduce beam exposure.

278 The 13-ID-E monochromator calibration provides a first derivative of the Fe *K*-edge peak
279 of iron foil at ~ 7110.7 eV, consistent with values determined by Kraft et al. (1996). We followed
280 the Fe-XANES measurement methodology outlined in Head et al. (2018), but with modified scan
281 times and energy ranges used to further identify and correct for beam damage. Two different
282 analytical setups were used: rapid pre-edge scans and slower full energy scans. For rapid scans,
283 the incident beam was scanned from 7092 – 7107 eV in 2.5 eV steps, from 7107 – 7119 eV in

284 0.1 eV steps, and from 7119 – 7144 eV in 0.05 \AA^{-1} (0.5 – 1.0 eV) steps (continuous steps rather
285 than discrete). Each scan step was 0.5 seconds (s) and the total scan time was 82 s, with ~10 s
286 delay prior to the next analysis for beamline adjustment and computational processing. The rapid
287 pre-edge scans quickly measure over a reduced energy range to minimize beam exposure to the
288 extent possible while still collecting spectra with high enough resolution for peak fitting in the
289 pre-edge region. The 82 s scan is much faster than typical Fe-XANES scan durations reported in
290 the literature, which usually range from 270 s to >700 s (4.5 to >10 minutes) (e.g., Cottrell et al.,
291 2009, 2018; Moussallam et al., 2016; Head et al., 2018; Gaborieau et al., 2020; Tassara et al.,
292 2020). The slower, full energy range scans measured from 7012 – 7102 eV in 2.5 eV steps, from
293 7102 – 7120 eV in 0.1 eV steps, and from 7120 – 7356 eV in 0.05 \AA^{-1} (0.5 – 3.0 eV) steps. Each
294 scan step time was either 0.5 or 1 s and total scan durations were 176 or 352 s. This full energy
295 range scan served as a higher-resolution scan of both the pre- and post-absorption edge regions,
296 which is similar to analytical procedures reported in other Fe-XANES studies and allowed
297 spectra to be normalized and assessed for mineral contamination.

298 Measured spectra were normalized to the incident flux ($K\alpha$ fluorescent intensity / incident
299 flux [I0]) and were fit using XAS viewer within the LARCH software package (Newville, 2013).
300 $\text{Fe}^{3+}/\Sigma\text{Fe}$ was calculated using relative pre-edge peak intensities following approaches described
301 in Cottrell et al. (2009). This approach uses the calculated centroid energy of the pre-edge
302 doublet, which is related to the $1s \rightarrow 3d$ electron transition, to determine glass $\text{Fe}^{3+}/\Sigma\text{Fe}$ based on
303 calibrations to standard glasses equilibrated at known $f\text{O}_2$ conditions and measured using
304 Mössbauer spectroscopy (Berry et al., 2003; Wilke et al., 2004; Cottrell et al., 2009). An energy
305 offset between our basaltic glass measurements and those used in the Fe-XANES calibration of
306 Cottrell et al. (2009) (due to monochromator calibrations and background subtractions during
307 peak fitting) was determined by comparing the Fe pre-edge centroid position of basaltic
308 reference glass LW_0 (Cottrell et al., 2009, 2018; Zhang et al., 2016, 2018) from the
309 Smithsonian Institution. The split of LW_0 glass analyzed here is embedded in the mount
310 NMNH 118279/IGSN NHB007V34, and is the same specimen as found in the mount with
311 catalog number NMNH 117393/IGSN NHB0073V8 (both available by request from the
312 Smithsonian Institution). The pre-edge centroid position of LW_0 was measured by Cottrell et
313 al. (2009) to have an energy of 7112.30 eV using the beamline configuration they described at
314 the National Synchrotron Light Source (Brookhaven National Laboratory). All Fe-XANES

315 spectra in figures and data tables throughout this manuscript are presented in energy units as-
316 measured at APS. However, when calculating iron valences in basaltic glasses, energy shifts of
317 +0.317 and +0.323 eV were respectively applied to iron pre-edge centroid positions for
318 measurement sessions 2018-3 and 2019-2 to provide consistency with centroid values measured
319 for LW_0 in Cottrell et al. (2009). Pre-edge peak fitting ranges were similarly adjusted from
320 Cottrell et al. (2009) to span an energy range of 7108.7 – 7116.7 eV, consistent with the
321 methodology discussed in Zhang et al. (2016). Within this fit window, the absorption baseline of
322 the main Fe *K* absorption edge was fit using a linear and a Lorentzian function, and the pre-edge
323 doublet was fit using two Gaussian functions (Cottrell et al., 2009). The centroid value of the
324 these two peaks was used to calculate $\text{Fe}^{3+}/\Sigma\text{Fe}$ using the Mössbauer-based calibration of Zhang
325 et al. (2018) for basaltic glasses.

326 For dacitic and rhyolitic glasses, average iron valence was calculated from a
327 parameterization of Fiege et al. (2017) for felsic glasses. No energy offsets were applied because
328 our measurements of the first derivative of the absorption edge of iron foil were consistent with
329 those of Fiege et al. (2017). Uncertainties in centroid values (± 1 SE), as detailed below, are
330 propagated through the basalt or rhyolitic calibrations to calculate uncertainties of $\text{Fe}^{3+}/\Sigma\text{Fe}$
331 calculations.

332

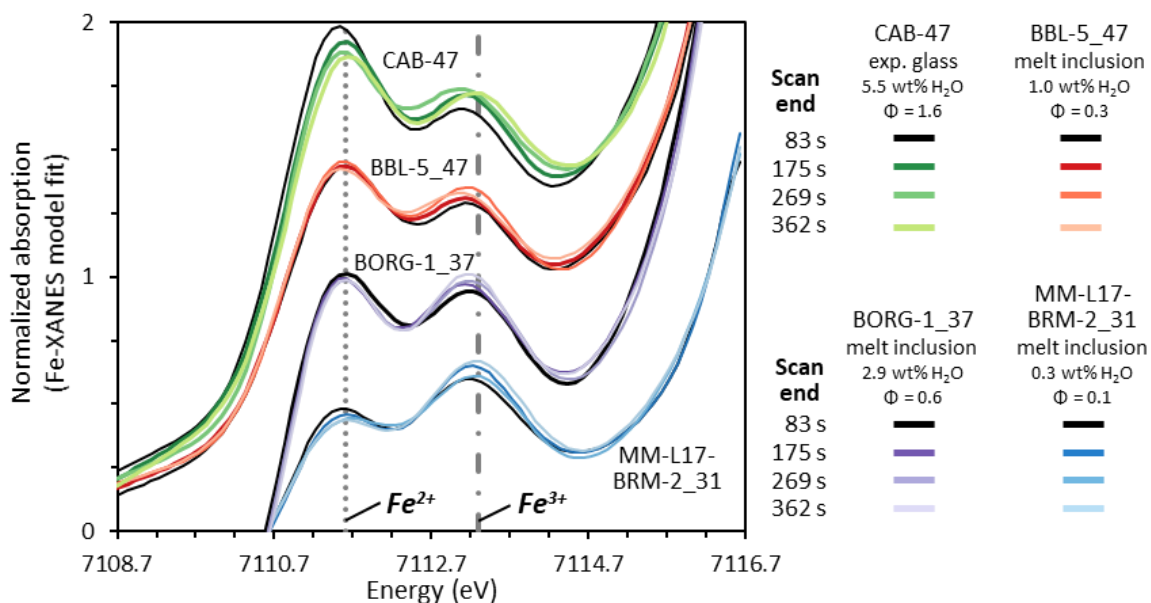
333 **2.2.1 Timescales of Fe-XANES beam damage**

334 Fe-XANES analysis of hydrous silicate glasses with a high intensity X-ray beam can
335 cause rapid photo-oxidation of Fe^{2+} to Fe^{3+} within the glass, creating large inaccuracies in
336 determining the initial $\text{Fe}^{3+}/\Sigma\text{Fe}$ values of glasses (Cottrell et al., 2018; Moussallam et al., 2019)
337 (Figure 2). The extent of this oxidation varies depending on glass composition and photon dose.
338 Beam-induced oxidation causes a shift in Fe-*K* α pre-edge peak intensities but does not produce
339 any uniquely identifiable spectral features. Consequently, it is impossible to know from a single
340 Fe-XANES analysis whether a sample had suffered from beam-induced photo-oxidation
341 (compare with S-XANES beam damage, which produced diagnostic spectral features, as
342 discussed in section 2.3). Therefore, samples must either be analyzed under carefully tested
343 analytical conditions to ensure that no significant beam damage occurs for the particular glass
344 composition and analysis duration, or a method must be employed that can identify and correct
345 for beam damage in each individual analysis spot. We emphasize the latter approach in this

346 study, presenting a method that allows us to reliably analyze small, hydrous glass inclusions with
 347 a relatively high-flux beam.

348 To identify and correct for beam damage within each analysis spot, we conducted
 349 multiple rapid scans of the Fe *K* pre-edge region to create a time series of progressive oxidation
 350 (Figure 2). These time series allow us to assess whether beam damage occurred during analysis
 351 and, if needed, enables us to calculate sample-specific corrections. For each analysis spot, we
 352 conducted 3 to 6 rapid pre-edge scans (82 s) followed by one full energy scan (176 or 352 s)
 353 across the entire Fe *K* absorption edge energy range. If pre-edge centroids calculated from the
 354 rapid scans did not show progressive oxidation over time, the spectra were merged together to
 355 form a single higher-resolution pre-edge spectrum. If changes in pre-edge centroid positions
 356 were observed, we use the time series of centroid positions to extrapolate the centroid back to
 357 $t=0$ s. We take this extrapolated value as the initial, ‘correct’ centroid position prior to beam
 358 exposure. This time-dependent correction approach is similar to methods commonly applied to
 359 electron microprobe measurements to account for alkali migration during electron beam
 360 excitement (Kuehn et al., 2011). A time-dependent approach has also been recently proposed for
 361 determining iron valence by electron microprobe measurements (Hughes et al., 2018).

362



363

364 **Figure 2.** Model fits to Fe-XANES pre-edge spectra for repeated rapid scans of experimental
 365 basaltic glass CAB-47 and of melt inclusions from the southern Cascades (CA, USA). Spectra of
 366 different samples have been vertically shifted for clarity. Progressive oxidation occurs during
 367 repeated rapid scans, as evidenced by the lighter colored lines. Samples have different initial

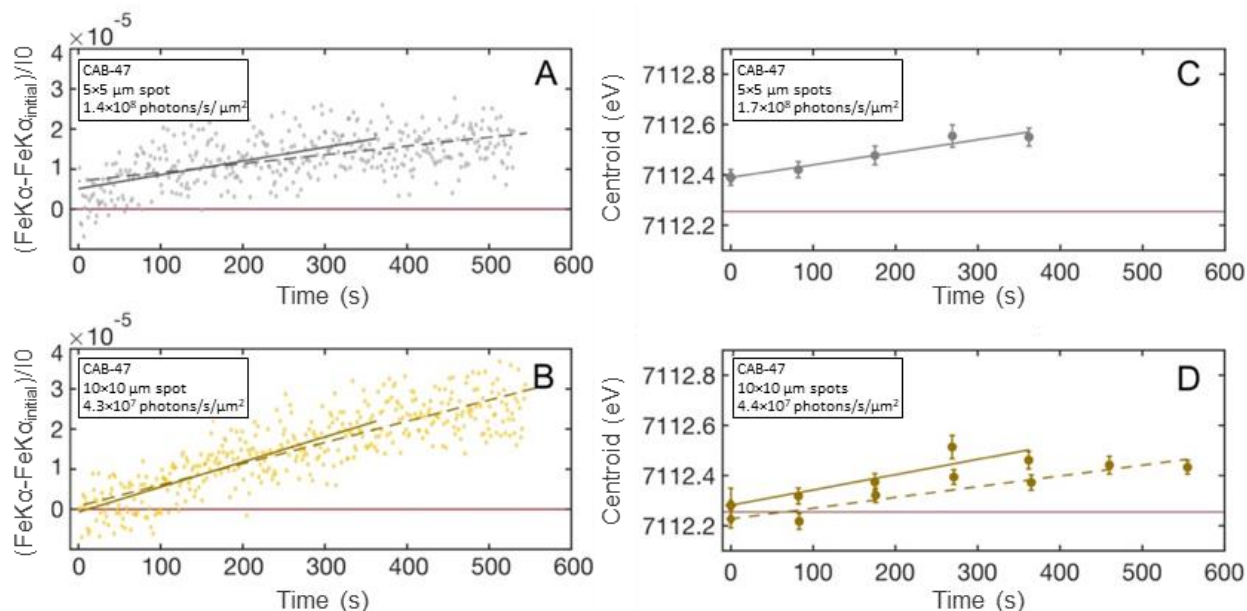
368 $\text{Fe}^{3+}/\Sigma\text{Fe}$ and H_2O contents, which affect the extent of beam-induced photo-oxidation.
369 Measurements were made with a $10\times 10\ \mu\text{m}$ beam and photon flux densities ranged from $2 -$
370 4×10^7 photons/s/ μm^2 . The lines labeled Fe^{2+} and Fe^{3+} refer to the approximate positions of the
371 first and second pre-edge doublet peaks.
372

373 X-ray induced photo-oxidation during Fe-XANES analysis can be difficult to identify,
374 partly because a large extent of the valence change occurs rapidly in the first minutes of analysis
375 (Cottrell et al., 2018; Moussallam et al., 2019). To ensure that our sequences of repeated rapid
376 scans adequately captured changes to centroid positions during the earliest stages of photo-
377 oxidation, we measured changes to the intensity of the 2nd pre-edge doublet (at 7113.2 – 7113.4
378 eV at APS) in single spots over 6 – 16 minutes. Such dwell tests measure the photo-oxidation of
379 the analyzed glass at a much finer temporal resolution than pre-edge scans allow (Shorttle et al.,
380 2015; Cottrell et al., 2018; Moussallam et al., 2019; Gaborieau et al., 2020). However, one
381 limitation to such single-energy dwell tests are that other simultaneously changing spectral
382 features cannot be detected. Additionally, one must assume that any changes in spectral
383 background during the measurement duration are negligible.

384 We conducted a set of dwell tests on an experimental basaltic glass (CAB-47, Weaver et
385 al. [2011]) (Figure 3A, B) with a high H_2O content (5.5 wt%) and a high proportion of Fe^{2+}
386 ($\sim 0.13\ \text{Fe}^{3+}/\Sigma\text{Fe}$). Sample CAB-47 shows larger degrees of beam-induced oxidation of iron
387 compared to the natural glasses studied here, likely due to its combined high H_2O and Fe^{2+}
388 contents (Cottrell et al. 2018). The calculated beam damage susceptibility index (Φ , where $\Phi =$
389 $\text{XHO}_{0.5} * \text{XFeO}/\text{XFeO}_{1.5}$), as described in Cottrell et al. (2018), is 1.6 for CAB-47 compared to
390 Φ of 0.1 – 0.7 for the various natural MI investigated in this study (Figure 5, Table 1). We
391 therefore use this highly beam damage-susceptible experimental glass to evaluate models for
392 correcting changing iron valence during Fe-XANES analysis.

393 To evaluate if time series of repeated rapid pre-edge scans (82 s durations, described
394 above) are sufficiently fast to capture photo-oxidation in CAB-47, we compared the pre-edge
395 rapid scan time series to the 2nd pre-edge doublet dwell tests in the same glass (Figure 3, Figure
396 A.1). It is assumed that the rate of change of the 2nd pre-edge doublet intensity scales with the
397 change in centroid value during time series analyses (Cottrell et al., 2018; Moussallam et al.,
398 2019). Dwell tests of the 2nd pre-edge doublet of CAB-47 with a photon flux density of $\sim 1.4\times 10^8$
399 photons/s/ μm^2 (analyzed with a $5\times 5\ \mu\text{m}$ spot size) show that substantial photo-oxidation occurs

400 in the first minute of analysis, with $\text{Fe}^{3+}/\Sigma\text{Fe}$ increasing from 0.13 to 0.19. Under these high
 401 photon flux densities, photo-oxidation progresses non-linearly (Cottrell et al., 2018; Moussallam
 402 et al., 2019; Figure 3, Figure A.1). The time series of repeated rapid pre-edge scans cannot
 403 capture this non-linear behavior that occurs in the initial 10s of seconds of analysis, and therefore
 404 cannot adequately characterize photo-oxidation at such high photon flux densities (Figure 3A,
 405 C). However, by decreasing the photon flux density to $\sim 4.3 \times 10^7$ photons/s/ μm^2 (using a 10×10
 406 μm spot size), dwell tests of CAB-47 show that photo-oxidation is slow enough that changes to
 407 both the 2nd pre-edge doublet intensity and centroid values can be adequately approximated by
 408 fitting a linear function to repeated rapid pre-edge scans (Figure 3B, D). Although photo-
 409 oxidation may remain non-linear in the initial minute of analysis even at this lower photon dose,
 410 the linear fit approximates the data within typical measurement uncertainty and is thus a
 411 reasonable approximation. The progression of photo-oxidation becomes more linear with further
 412 decreased photon flux densities (Figure A.1).
 413



414
 415 **Figure 3.** (A, B) Intensities of the 2nd pre-edge doublet as a function of time in experimental
 416 glass CAB-47 measured with photon flux densities of 1.4×10^8 and 4.3×10^7 photons/s/ μm^2 (5×5
 417 μm and $10 \times 10 \mu\text{m}$ respective spot sizes). Gray and yellow lines are linear regressions through
 418 data from 0 to 362 s (solid) or 0 to 537 s (dashed). Fe-K α /10 initial intensity (red horizontal line)
 419 is taken as the average of the first 5 analyses. (C, D) Pre-edge centroid positions calculated from
 420 repeated rapid scans (see Figure 2) for experimental glass CAB-47 with photon flux densities of
 421 1.7×10^8 photons/s/ μm^2 ($5 \times 5 \mu\text{m}$ spot size; one time series) and $\sim 4.4 \times 10^7$ photons/s/ μm^2 (10×10
 422 μm spot size; two time series). Each circle is a centroid value calculated from one pre-edge scan

423 with error bars representing ± 1 SE of centroid fits to each scan. Diamonds at $t=0$ s are the
424 intercept of linear regressions to each time series and are taken to be beam damage corrected
425 centroid values. Error bars on the $t=0$ s centroid positions represent ± 1 SE of the time series
426 linear regression. Red lines in panels *C* and *D* are the estimated initial centroid value, which is
427 taken as the average beam damage corrected centroid values for the two $10 \times 10 \mu\text{m}$ analysis time
428 series (panel *D*). Gray and yellow lines are linear regressions through centroid values from 82 to
429 362 s (solid) or 82 to 537 s (dashed). Centroid values in *C* and *D* have been shifted by $+0.32$ eV
430 for consistency with the LW_0 centroid position reported by Cottrell et al. (2009).
431

432 The same dwell tests were conducted using similar photon densities on another
433 experimental hydrous basaltic glass (CAB-33, 7.2 wt% H_2O , $\Phi = 1.8$; Weaver et al., 2011) and
434 on a moderately hydrous natural obsidian pyroclast from Mono-Inyo Craters (CA, USA) (P2-F,
435 ~ 2.2 wt% H_2O ; Barnes et al., 2014; Watkins et al., 2017; Table 1) Observed changes to the 2nd
436 pre-edge doublet intensity in these glasses were similar to those measured in CAB-47 (Figure
437 A.1), suggesting that the time series correction approach can be applied across a range of basalt
438 to rhyolite glass compositions, including hydrous samples that are highly susceptible to photo-
439 oxidation.

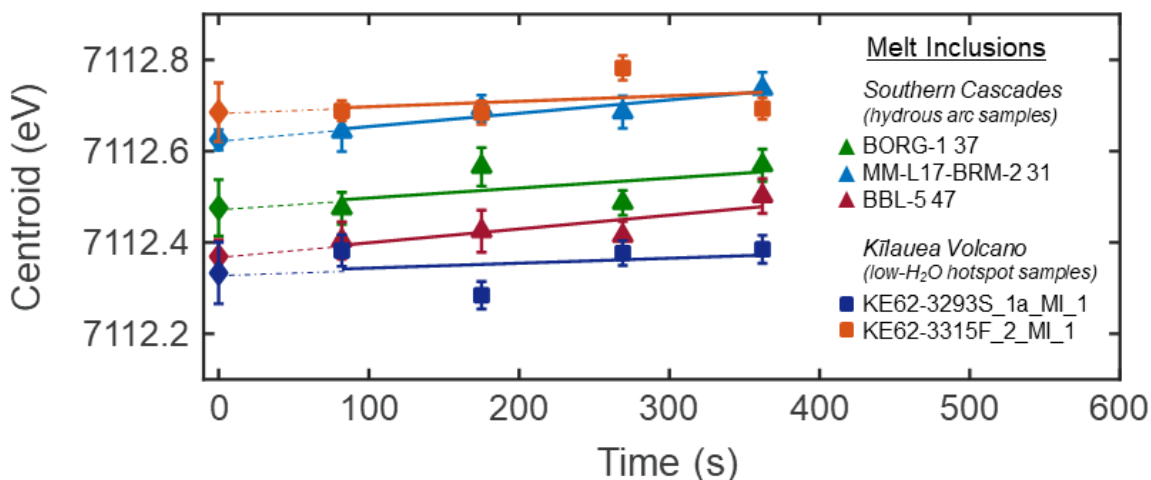
440

441 **2.2.2 Applying the Fe-XANES beam damage correction technique to natural melt**

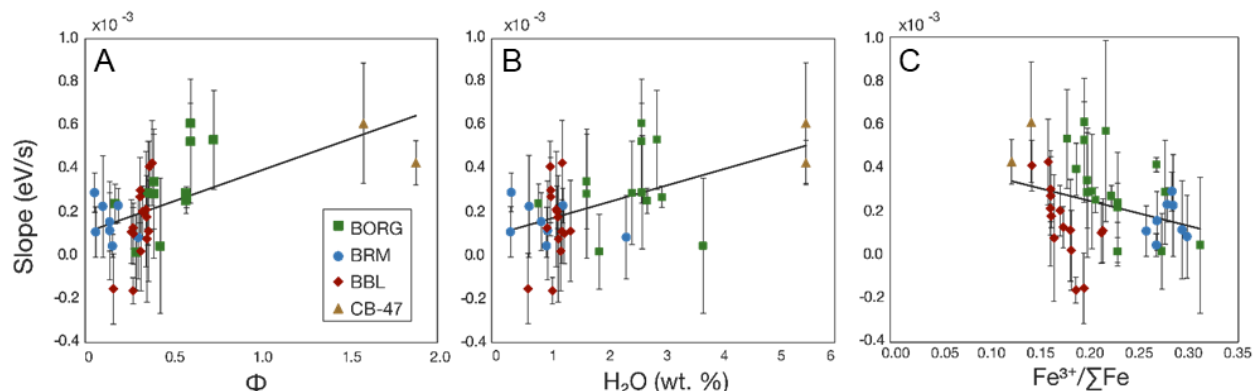
442 **inclusions**

443 Because glass CAB-47 is more susceptible to beam damage than most MI and matrix
444 glasses, changes to pre-edge centroids in most natural samples analyzed under the same
445 conditions ($\sim 3.0 \times 10^7$ photons/s/ μm^2) can also be approximated with a linear function. Hydrous
446 basaltic MI from the southern Cascades arc (0.3 – 3.7 wt% H_2O , $\Phi = 0.1 - 0.7$) show consistent
447 increases in pre-edge centroid values over the course of several repeated rapid scans, indicating
448 progressive photo-oxidation (Figure 4, Table 1). In contrast, basaltic MI from Kīlauea Volcano
449 (HI, USA) do not show time-dependent changes to pre-edge centroid values, as expected based
450 on their low H_2O contents and low beam damage susceptibilities (0.1 – 0.3 wt% H_2O , $\Phi \leq 0.1$)
451 (Figure 4, Table 1). The slopes of linear regressions to centroid time series (i.e., the rate of
452 photo-oxidation) are inversely correlated with calculated initial $\text{Fe}^{3+}/\Sigma\text{Fe}$ and are positively
453 correlated with H_2O contents of each glass (Figure 5, Figure A.2). These observations are
454 consistent with the findings of Cottrell et al. (2018) that beam damage occurs more readily in
455 reduced and/or hydrous glasses.

456 To apply time series corrections in beam damage-susceptible samples, linear regressions
 457 using 4 rapid pre-edge scans are generally sufficient to correct to initial (t=0 s) centroid
 458 positions. However, using up to 6 pre-edge scans can provide an improved regression fit, as
 459 increased scans minimize the leverage of anomalously noisy scans in the regression (Figure 3D).
 460 Uncertainties in restored initial centroid positions were assessed by calculating the standard error
 461 of regression for each time series and by calculating the standard deviation of time series linear
 462 fits using a Monte Carlo method that incorporates the standard error of each individual centroid
 463 fit (Browaeys, 2021). For the analytical conditions used in this study, these two approaches yield
 464 similar uncertainty estimates for the t=0 s centroid positions (Figure A.3). Weighting the linear
 465 regressions by the inverse of the squared standard deviation of each measurement's uncertainty
 466 also yields similar linear fits and standard error estimates for t=0 s centroid values. In time series
 467 with substantial scatter in centroid positions, the standard error of linear regressions is generally
 468 larger than the Monte Carlo-derived uncertainty estimates (Figure A.3). We therefore use the
 469 standard error of unweighted linear regressions to estimate uncertainties in the restored t=0 s
 470 centroid positions, as this is the simplest and generally most conservative approach.
 471



472
 473 **Figure 4.** Fe $K\alpha$ pre-edge centroid positions calculated from repeated rapid scans of MI from the
 474 southern Cascades (triangles) and from Kīlauea Volcano (squares). Symbols are the centroid
 475 values calculated from individual pre-edge scans and error bars represent ± 1 SE for each centroid
 476 fit. Lines are linear regressions through centroid values from 82 to 362 s. Diamonds at t=0 s are
 477 the intercept of each regression (dashed lines), taken to be the beam damage corrected centroid
 478 position. Error bars on diamonds represent ± 1 SE of the time series linear regression. Analyses
 479 used a $10 \times 10 \mu\text{m}$ spot size, which resulted in photon flux densities of $3 - 5 \times 10^7$ photons/s/ μm^2 .
 480 All centroids have been shifted by +0.32 eV for consistency with the LW_0 centroid position
 481 reported by Cottrell et al. (2009).



482
 483 **Figure 5.** Slopes of linear regressions through centroid value time series for individual glasses
 484 plotted as a function of (A) beam damage susceptibility index ($\Phi = X\text{HO}_{0.5} * X\text{FeO}/\text{FeO}_{1.5}$) as
 485 defined in Cottrell et al. (2018), (B) H_2O content, and (C) initial $\text{Fe}^{3+}/\Sigma\text{Fe}$. Melt inclusions from
 486 southern Cascades cinder cones (BORG, BRM, BBL) and experimental glass analyses (CAB-47)
 487 are grouped by color. Gray lines are linear regressions through analysis spots from all natural and
 488 experimental samples.

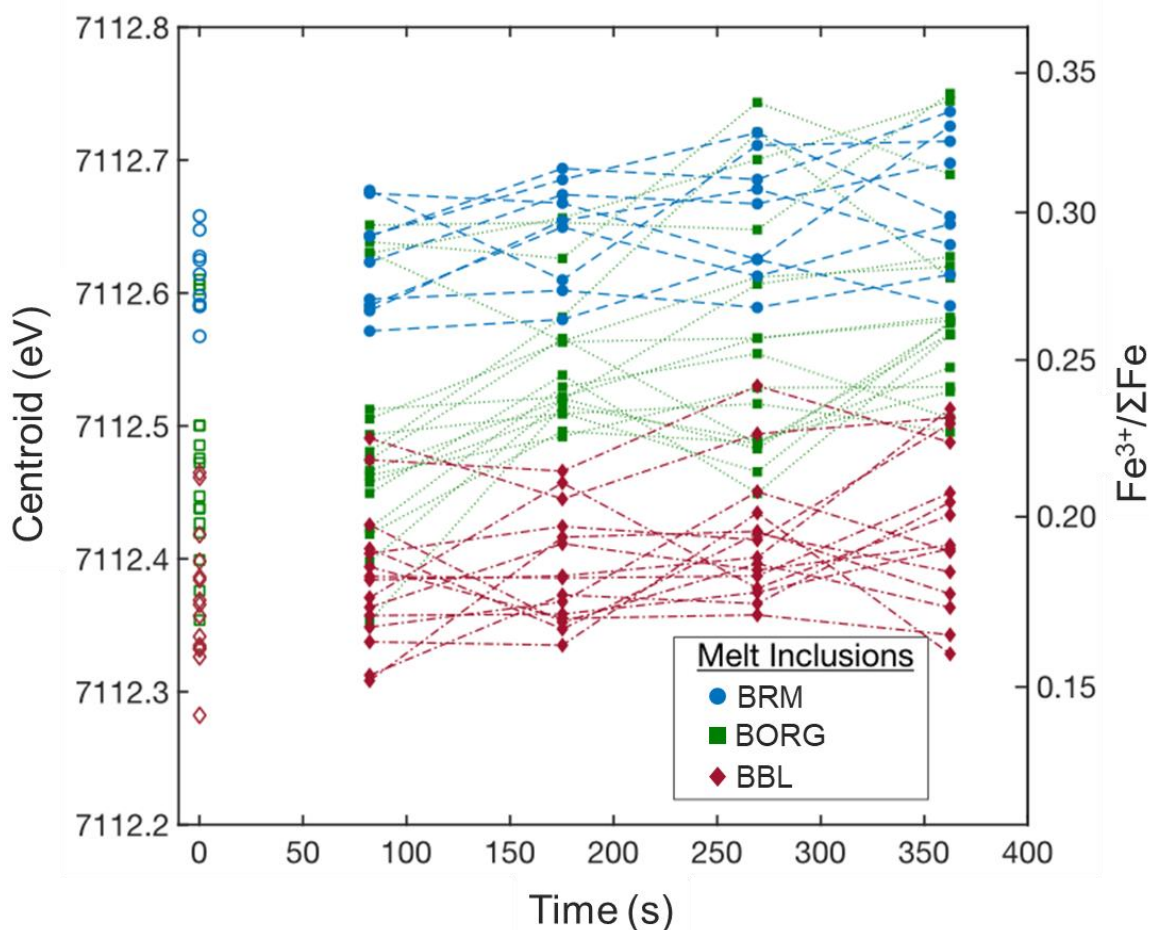
489
 490 For hydrous basaltic MI from the southern Cascades, the average 1 standard error of
 491 regression for corrected $t=0$ s centroid values is ± 0.04 eV, or ± 0.02 $\text{Fe}^{3+}/\Sigma\text{Fe}$ when propagated
 492 through the calibration of Zhang et al. (2018) (note that curvature of the calibration function
 493 increases $\text{Fe}^{3+}/\Sigma\text{Fe}$ uncertainties in more oxidized glasses). This uncertainty is only slightly
 494 larger than the average standard error of centroid value fits of our higher resolution full length
 495 scans (± 0.03 eV; ± 0.01 $\text{Fe}^{3+}/\Sigma\text{Fe}$), and is much smaller than the ~ 0.15 variation in $\text{Fe}^{3+}/\Sigma\text{Fe}$
 496 measured in basaltic arc MI globally (Kelley and Cottrell, 2009; Brounce et al., 2014; Muth and
 497 Wallace, 2021). Regressions on replicate analyses within the same MI yield corrected centroid
 498 positions that are within error of each other (Figure A.4), indicating that our correction approach
 499 is reasonably accurate.

500
 501 **2.2.3 Discussion and summary**

502 Although the time-dependent beam damage correction approach introduces some
 503 imprecision, it ensures that data sets are not systematically biased to higher calculated $\text{Fe}^{3+}/\Sigma\text{Fe}$
 504 values due to uncorrected photo-oxidation. In analyses of basaltic MI from the southern
 505 Cascades (measured with photon flux densities of $1 - 5 \times 10^7$ photons/ $\mu\text{m}^2/\text{s}$), the difference
 506 between corrected and uncorrected centroid positions is large (Figure 6). On average, centroid
 507 values measured after 362 s of analysis are 0.09 eV higher than $t=0$ s corrected centroid values.

508 This means that despite measures taken to lower the photon flux, had we analyzed these hydrous
 509 MI with more typical 10-minute duration scans (where the pre-edge region is measured within
 510 the first ~6 minutes) our analyses would have overestimated melt $\text{Fe}^{3+}/\Sigma\text{Fe}$ by ~0.036. This
 511 would correspond to an overestimation of the $f\text{O}_2$ by 0.5 log units for basalt at 1150 °C and 400
 512 MPa, according to the model of Kress and Carmichael (1991).

513
 514
 515



516
 517 **Figure 6.** Fe- $K\alpha$ pre-edge centroid positions through time calculated from repeated pre-edge
 518 scans for individual southern Cascades MI. Dashed lines connect centroids calculated from four
 519 consecutive rapid scans of the same analysis spot, and open symbols at $t=0$ s are the corrected
 520 initial centroids. Centroid time series measurements are plotted at the end time of each scan.
 521 Right vertical axis is the calculated $\text{Fe}^{3+}/\Sigma\text{Fe}$ from centroid values using the calibration of Zhang
 522 et al. (2018). All centroids have been shifted by +0.32 eV for consistency with the LW_0
 523 centroid position reported by Cottrell et al. (2009).
 524

525 In summary, photo-oxidation during Fe-XANES measurements can cause large
526 systematic biases toward higher calculated $\text{Fe}^{3+}/\Sigma\text{Fe}$ in beam-sensitive glasses, which can
527 significantly affect geologic interpretations of redox conditions (Cottrell et al., 2018;
528 Moussallam et al., 2019). Taking measures to mitigate beam damage through reduced X-ray flux
529 density (where possible) and/or by applying analysis-specific time-dependent corrections
530 described here is critical for accurate interpretation of Fe-XANES measurements in beam-
531 sensitive glasses, such as hydrous arc basalts. We present a time-dependent correction method
532 and set of analysis conditions that should enable beam damage identification and correction in
533 most natural silicate glasses at even relatively high photon flux densities (10^7 – 10^8
534 photons/s/ μm^2). However, photo-oxidation during analysis is a function of glass composition
535 (including H_2O content and initial $\text{Fe}^{3+}/\Sigma\text{Fe}$), photon flux density, and duration of analysis, and
536 therefore depends on the specific sample and beamline properties. Best practices during Fe-
537 XANES analysis of glasses would include explicitly testing (via 2nd pre-edge multiplet dwell
538 tests) whether repeated rapid pre-edge scans sufficiently correct photo-oxidation for the
539 particular beamline conditions and sample composition being analyzed.

540

541 **2.3 Identifying and correcting S-XANES beam damage**

542 S-XANES measurements use lower X-ray energies than Fe-XANES (~2480 eV vs ~7110
543 eV, respectively) and therefore have smaller absorption lengths than Fe-XANES measurements.
544 At S-XANES energies, 95% of X-ray energy is absorbed within the upper ~15 μm of glass
545 (Wilke et al., 2011) (Figure 1A). The MI analyzed here are thicker than 15 μm so that doubly
546 intersecting the inclusions was not necessary for S-XANES analyses. Additionally, most host
547 minerals contain negligible sulfur compared to MI (Callegaro et al., 2020) so that beam overlap
548 of the host mineral is less of a concern than for Fe-XANES analyses, where iron signal
549 contribution from the host phase can be significant. Consequently, larger X-ray analysis
550 footprints can generally be used for S-XANES, which reduces X-ray dose and thereby
551 ameliorates some of the beam damage potential. However, when analyzing sulfur-poor MI
552 (<~400 ppm S), even slight contributions from the host phase might be significant relative to the
553 low-sulfur glass signal, and beam overlap of the host phase should be avoided. Additionally,
554 cracks and surface contaminants (e.g., oils) may be present on prepared surfaces, both of which

555 can contain undesired sulfur-bearing material (Brounce et al., 2019). Consequently, smaller
556 beam footprints for S-XANES remain more versatile for analysis of MI (particularly for low-
557 sulfur samples) because of the ability to avoid contamination from host minerals or from surface
558 aberrations.

559 Sulfur in silicate melts occurs as S^{2-} (sulfide complexes) or S^{6+} (sulfate complexes;
560 $S^{(VI)}O_4^{2-}$) but does not naturally occur as S^{4+} (sulfite complexes; $S^{(IV)}O_3^{2-}$) at the limit of
561 detection by XANES (Backnaes et al., 2008; Wilke et al., 2008, 2011). The main absorption
562 peak of S^{2-} complexes in glasses occurs over a broad energy range centered at ~ 2476 eV, and the
563 absorption peak of S^{6+} complexes occurs at ~ 2482 eV (Li et al., 1995; Paris et al., 2001; Bonnin-
564 Mosbah et al., 2002; Wilke et al., 2008; Métrich et al., 2009; Jugo et al., 2010). In Fe-bearing
565 natural glasses, S-XANES beam damage typically manifests as photo-reduction of S^{6+} to S^{4+}
566 (Wilke et al., 2008). The absorption peak for sulfite occurs at 2477.5 eV (note that the rapid
567 oxidation of sulfite at the surface causes a 2482 eV sulfate peak to also be present in the spectra
568 of most sulfite reference materials) (Métrich et al., 2002, 2009; Bonnin-Mosbah et al., 2002;
569 Fleet et al., 2005; Wilke et al., 2008; Jugo et al., 2010). The 2477.5 eV sulfite peak is a unique
570 spectral signal to recognize S^{4+} speciation and thereby can be used to identify measurements that
571 have undergone beam damage (Wilke et al., 2008; Métrich et al., 2009; Moussallam et al., 2014).
572 Beam damage is therefore more easily detected in S-XANES than in Fe-XANES, and time-
573 dependent corrections to $t=0$ s are not necessary because all observed S^{4+} is generally attributable
574 to beam-induced reduction of sulfur. Photo-reduction of S^{6+} has also been observed during
575 electron microprobe (EPMA) S- $K\alpha$ wavelength scans (Wilke et al., 2008). However, photo-
576 oxidation of S^{2-} to S^{4+} or to S^{6+} has been documented by other EPMA studies (Wallace and
577 Carmichael, 1994; Rowe et al., 2007) and during extremely long duration XANES measurements
578 (20 – 80 minutes) of highly alkalic glasses from Mt. Erebus (Antarctica) (Moussallam et al.,
579 2014). The predominance of sulfur photo-reduction during XANES analyses of natural glasses
580 suggests that different mechanisms of sulfur beam damage may occur under electron
581 bombardment compared to X-ray irradiation, and potentially also during X-ray irradiation of
582 alkali-rich glasses (Hughes et al., 2020).

583 The parameters influencing photo-reduction (S^{6+} to S^{4+}) in silicate glasses during S-
584 XANES irradiation are imprecisely known. In contrast to Fe-XANES beam damage (Cottrell et
585 al., 2018), H_2O content does not appear to be a critical control on S-XANES beam damage (see

586 section **2.3.3**), and the compositional dependence of S-XANES beam damage susceptibility has
587 not been thoroughly examined. It is consequently difficult to currently predict whether any
588 particular sample will be susceptible to S-XANES beam damage. Therefore, as with iron beam
589 damage, it is important to be able to account for beam damage within each individual
590 measurement rather than applying generalized corrections to an entire sample suite.

591 Our approach in managing and correcting S-XANES beam damage is similar to that for
592 reducing Fe-XANES beam damage, namely minimizing pre-analysis X-ray irradiation,
593 decreasing photon dose as much as possible while maintaining sufficient signal, and using repeat
594 rapid scans to observe beam-induced changes in sulfur speciation. Where S-XANES photo-
595 reduction is observed, we correct affected spectra by calculating the peak area of the beam
596 damage-induced S⁴⁺ signal and restoring this to original S⁶⁺ intensity via a calibrated conversion
597 factor (details below).

598

599 **2.3.1 S-XANES analytical conditions**

600 S-XANES measurements at APS GSECARS beamline 13-ID-E were conducted in
601 fluorescence mode and within a He-environment to minimize atmospheric absorption of the X-
602 ray fluorescent signal. Incident beam flux ranged from ~1 – 50×10⁹ photons/s for S-XANES
603 analyses, which was purposely lowered from the maximum possible flux to reduce rates of beam
604 damage. Repeat measurements of sulfate within Scotch[®] tape during four analytical sessions
605 between 2017 – 2020 indicate a consistent S⁶⁺ peak position of 2481.8 eV. The sulfate peak
606 position in crystalline hauyne measured by Jugo et al. (2010) at the European Synchrotron
607 Radiation Facility's beamline ID21 is +1 eV relative to sulfate measurements at APS beamline
608 13-ID-E, due to differences in monochromator calibration (Head et al., 2018). Thus, all the Jugo
609 et al. (2010) values presented in figures and data tables have been shifted by -1 eV for
610 consistency.

611 As with our Fe-XANES beam damage correction approach, we conducted repeat rapid
612 scans to identify S-XANES beam damage and, if necessary, applied sample-specific corrections.
613 Sulfur *K*-edge spectra were collected by scanning the incident beam from 2437 – 2467 eV in 2.5
614 eV steps, from 2467 – 2487 eV in 0.1 eV steps, and from 2487 – 2622 eV in 1.5 eV steps. Short
615 analysis times of either 0.5 or 1.0 s per step bin were used (continuous steps rather than discrete)
616 for rapid scans with total durations of 154 or 308 s, respectively. Three repeat scans were

617 typically conducted for each analysis spot, with cumulative measurement times of ~8 – 15
618 minutes per location. If S⁴⁺ peak growth was identified during successive scans, only the first
619 scan was used to quantify sulfur speciation, as this scan would have undergone the least S⁶⁺ to
620 S⁴⁺ photo-reductive beam damage. If no S⁴⁺ peak ingrowth was observed, the repeat scans were
621 merged to improve signal quality.

622 In beam-damaged samples, S⁶⁺ to S⁴⁺ photo-reduction can be corrected by restoring the
623 S⁴⁺ 2477.5 eV peak intensity back to a S⁶⁺ signal. This correction requires knowing an
624 appropriate signal intensity scaling factor to restore a S⁴⁺ signal to the original S⁶⁺ intensity.
625 Konecke et al. (2017) and Nash et al. (2019) apply S-XANES beam damage corrections by
626 assuming a 1:1 intensity scaling between S⁴⁺ and S⁶⁺ peaks. However, in the absence of direct
627 evidence, the accuracy of this assumed 1:1 scaling relationship of fluorescent energy outputs is
628 uncertain. To determine how the loss of S⁶⁺ intensity relates to the growth of S⁴⁺, and therefore
629 how to calculate an appropriate signal intensity scaling factor between these peak intensities, we
630 conducted a series of measurements on a hydrous, sulfate-dominated, sulfur-rich experimental
631 basaltic glasses from Chowdury and Dasgupta (2019) (Table 1). The large area of this
632 experimental glass allowed a series of measurements with multiple spot sizes (2×2, 10×10,
633 20×20, and 50×50 μm) to observe varying degrees of beam damage under photon densities
634 ranging from 6.9×10⁶ – 1.1×10¹⁰ photons/s/μm². The sulfate-only initial composition of this
635 oxidized glass made the identification of S⁴⁺ peak ingrowth obvious. With repeat measurements,
636 we are able to track the ingrowth of the S⁴⁺ 2477.5 eV peak (hereafter the “S⁴⁺ peak”) at the
637 expense of the S⁶⁺ 2481.3 – 2482 eV peak. We can thereby quantify how the S⁴⁺ peak intensity
638 relates to the loss of S⁶⁺ intensity, and how consistent the S⁴⁺ to S⁶⁺ intensity scaling relationship
639 is with increasing degrees of beam damage.

640

641 **2.3.2 Quantifying S-XANES spectra via peak fitting**

642 Determining the relationship between S⁴⁺ signal growth and S⁶⁺ signal loss during S-
643 XANES beam damage requires a consistent peak fitting method to quantify the change in
644 absorption intensities. Peak fitting approaches to S-XANES spectra have been employed by
645 other researchers (Manceau and Nagy, 2012; Konecke et al., 2017; Nash et al., 2019), but have
646 not been described or calibrated in silicate glasses at the level of detail required to be fully
647 reproducible. We therefore establish a new peak fitting calibration based on the dataset used by

648 Jugo et al. (2010) to originally define a calibration relating S-XANES signal intensities to sulfur
649 speciation. S-XANES spectra of silicate glasses are produced by a mixture of X-ray photon
650 absorptions by S^{2-} , S^{4+} , and S^{6+} species, and by S^{1-} and S^{2-} sulfide complexes (Paris et al., 2001;
651 Fleet et al., 2005; Métrich et al., 2009). Jugo et al. (2010) empirically determined a relationship
652 of S^{2-} and S^{6+} X-ray absorption intensities to sulfur speciation using a set of experimental glasses
653 by integrating all signal within energy ranges relating to S^{2-} and S^{6+} peaks (2474.7 – 2479 eV and
654 2480.5 – 2483 eV, respectively; Jugo et al. [2010] ranges have been shifted by -1 eV). However,
655 the S^{4+} absorption peak (2476.8 – 2477.6 eV) occurs within the broad S^{2-} energy range.
656 Consequently, the Jugo et al. (2010) approach would inappropriately include any photo-
657 reduction induced S^{4+} signal intensity as S^{2-} intensity. Our peak fitting approach differentiates S^{2-}
658 , S^{4+} , and S^{6+} absorption intensities, enabling us to quantify beam damage by isolating S^{4+} from
659 the S^{2-} peak. We can then restore the S^{4+} photo-reduction signal to an original S^{6+} intensity to
660 calculate the undamaged sulfur speciation of the glass.

661 Our S-XANES peak fitting method again uses the spectral fitting program XAS viewer
662 (Newville, 2013) to correct for instrument deadtime and to fit the S-XANES data. Measured
663 spectra were first scaled by the Si- $K\alpha$ signal intensity, to avoid aberrations in incident beam
664 intensity over the analysis energy range due to possible contaminants within the beamline optics.
665 Following the approach of Jugo et al. (2010) and Anzures et al. (2020), we then normalize each
666 spectrum so that the energy range containing pre-edge features begins at zero intensity (~2467
667 eV), and the post-edge signal intensity is 1 (>2510 eV). This is done by defining a linear relation
668 in the low energy range (~2441 – 2467 eV), and flattening the high energy range (~2525 – 2611
669 eV) to scale the spectra to between 0 – 1 (Ravel and Newville, 2005; Anzures et al., 2020). These
670 energy ranges for normalization are guidelines that should be slightly modified as necessary if
671 anomalous data points are present for particular scans. However, sulfide X-ray absorption begin
672 at energies just above 2467, so the pre-edge normalization range should be kept below this
673 energy. The normalized post-edge spectrum is fit using an error function and a broad Gaussian,
674 which together define the background. The center point of the error function is fixed and the
675 width of the high-energy Gaussian is constrained to maintain a consistent background fitting
676 approach for all spectra (Table 2).

677 Assessing S-XANES spectra of >100 reduced and oxidized glass analyses across a
678 compositional range from basaltic to rhyolitic (Table 1; **Data supplement**), we identify the

679 energy ranges of five peaks within the S-K α absorption region. We distinguish four absorption
 680 peak ranges that have been recognized as corresponding to sulfide complexes, and S²⁻, S⁴⁺, and
 681 S⁶⁺ species (Wilke et al., 2008, 2011; Métrich et al., 2009; Jugo et al., 2010; Head et al., 2018)
 682 (Table 2). We additionally identify an absorption peak between 2483.5 – 2486 eV, which is
 683 slightly higher energy than the main S⁶⁺ peak. This 2483.5 – 2486 eV energy peak was similarly
 684 identified by Konecke et al. (2017), who refer to it as the sulfur “ionization peak”, a term we
 685 adopt here. The sulfur-ionization peak intensity seems partially correlated to S⁶⁺ intensity, but is
 686 also present in S²⁻-dominated spectra. After normalizing the spectra, we simultaneously fit the
 687 background with an error function and Gaussian and fit five separate Gaussian functions for each
 688 of the sulfur absorption features (Figure 7, Figure A.6). Table 2 provides the energy ranges and
 689 peak width tolerances for fitting each spectral feature. These fitting ranges have been established
 690 to provide flexibility in fitting slight differences in peak energies occurring across a range of
 691 compositions and oxidation states, while maintaining peak positions that accurately correspond
 692 to the specific sulfur features (important for overlapping features such as the S²⁻ and S⁴⁺ peaks,
 693 and the S⁶⁺ and ionization peaks).

694

695 **Table 2.** Peak definitions and fit parameters used for quantification of normalized S-XANES
 696 spectra intensities using the XAS Viewer spectral fitting program (Newville, 2013). See **Data**
 697 **supplement** for example peak fit models.

S-XANES feature	function type / name	peak center bounds (eV)	peak sigma bounds (width)	peak amplitude bounds
<i>overall fit ranges</i>				
peak fit range	-	2455 – 2550	-	-
pre-edge fit range	-	2466 – 2487	-	-
<i>background fitting</i>				
baseline error function	error1	2485 (fixed)	8 (fixed)	0 – 1.1
baseline Gaussian	gauss1	2493 – 2500	0 – 10	0 – 15
<i>Sulfur speciation peaks</i>				
sulfide complexes	gauss2	2465 – 2470	0 – 1	0 – ∞
S ²⁻ (sulfide in glass)	gauss3	2475.3 – 2477	2 – 4	0 – ∞
S ⁴⁺ (sulfite)	gauss4	2476.8 – 2477.7	0.1 – 1	0 – ∞
S ⁶⁺ (sulfate)	gauss5	2480 – 2482.3	0.1 – 3	0 – ∞
sulfur ionization peak	gauss6	2483.5 – 2486	0 – 4	0 – ∞

698

699 To relate the relative fitted peak areas to sulfur speciation, we calibrate our peak fitting
700 method to experimental hydrous basaltic glasses presented in Jugo et al. (2010). Following the
701 same approach as Jugo et al. (2010), we use their completely S²⁻-bearing and completely S⁶⁺-
702 bearing experimental glasses as reduced and oxidized end-members, and apply linear
703 combination fitting of these end-members to produce representative mixed speciation spectra
704 (Figure A.5). Complete details are provided in the **Supplementary information**.

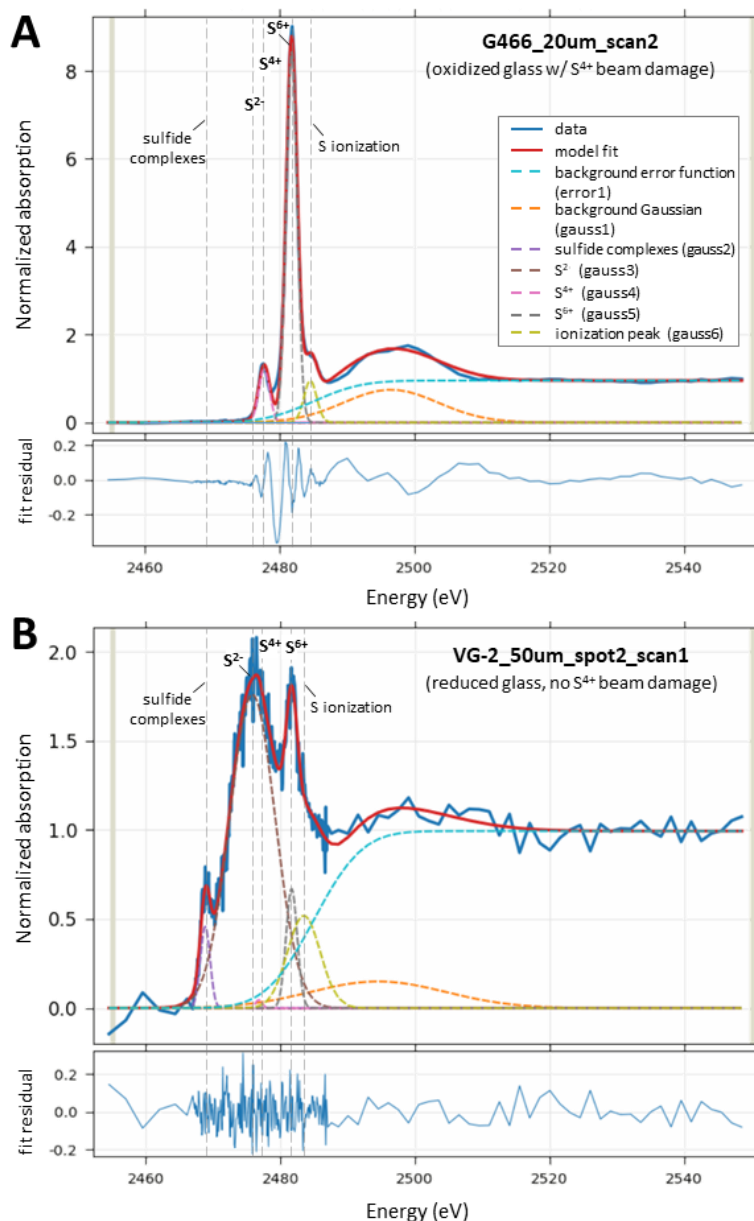
705 Jugo et al. (2010) focus their S-XANES calibration on only S²⁻ and S⁶⁺ peak intensities,
706 and do not include signals from lower energy sulfide-complexes or higher energy features
707 beyond the S⁶⁺ peak. We follow this approach, and although we fit all spectral features in the
708 calibration glasses, we use only the S²⁻ and S⁶⁺ peak areas to quantify the sulfur speciation in
709 glasses (Figure 7, Figure A.6). Jugo et al. (2010) describe an exponential function to relate S²⁻
710 and S⁶⁺ peak intensities to sulfur speciation, however we find that the following empirical
711 polynomial relationship is more appropriate for our peak fitting method (Figure A.7):

$$S^{6+}/\Sigma S = 0.1733 * (I[S^{6+}]/\Sigma I[S^T])^2 + 0.8343 * (I[S^{6+}]/\Sigma I[S^T]), [Eq. 1]$$

712 where S⁶⁺/ΣS is the fraction of S⁶⁺ out of total sulfur in the glass, and I[S⁶⁺]/ΣI[S^T] is the
713 XANES-measured S⁶⁺ intensity (Gaussian peak area) out of the combined total intensities of the
714 S⁶⁺ peak and the broad S²⁻ peak (I[S⁶⁺] + I[S²⁻] = I[S^T]). This peak fitting approach accurately
715 reproduces observations from additional glasses synthesized by Jugo et al. (2010) across a range
716 of fO₂ and sulfur speciation (Figure A.8). We therefore conclude that our peak fitting approach is
717 similar to the calibration (and this compatible with the thermodynamic relations) originally
718 described by Jugo et al. (2010), while additionally allowing the quantification of a S⁴⁺ peak. We
719 note that our method is subject to the same limitations as the Jugo et al. (2010) approach,
720 namely, that the linear end-member mixing approach to calibrate mixed sulfur speciation melts is
721 valid. Additional uncertainty arises from inconsistencies with normalizing S-XANES spectra,
722 which can be challenging in sulfur-poor glasses. Unfortunately, raw S-XANES spectra are
723 seldom published, which precludes assessing consistency in normalization approaches between
724 studies. For reproducibility of spectral processing by future workers, it is important that both the
725 raw and the normalized/flattened S-XANES data be made available (see **Data supplement**)
726 (Rose-Koga et al., 2021).

727
728 The average precision of our S-XANES peak fitting method, based on multiple analyses
729 in single MI and within regions of mid-ocean ridge basalt (MORB) glasses, is ±7% relative (2

730 RSE, 19 analyses in glasses ranging from 0.07 to 0.85 $S^{6+}/\Sigma S$; see **Data supplement**). When
 731 considering further uncertainties in the peak fitting calibration and from the non-uniqueness of
 732 spectra normalization (particularly in signal-limited samples), we assume the total accuracy of
 733 this method to be better than $\pm 10\%$ relative.
 734



735
 736 **Figure 7.** (A) Example S-XANES peak fitting to oxidized experimental glass G466. This
 737 spectrum is the 2nd of 3 repeat scans with a 20×20 μm beam (photon flux density of 1.1×10^8
 738 photons/s/ μm^2) and shows a dominant S⁶⁺ peak (2480 – 2482.3 eV) and a substantial beam
 739 damage-induced S⁴⁺ peak (2476.8 – 2477.7 eV). No S²⁻ intensity is observed. The fit residual
 740 shows slight remaining unfit structure. (B) Example S-XANES peak fitting of reduced VG-2

741 MORB glass analyzed using a 50×50 μm beam (photon flux density of 6.2×10⁶ photons/s/μm²).
 742 The noisier spectrum is due to lower sulfur content in VG-2 than G466, as well as a difference in
 743 vertical scale. A main glassy S²⁻ peak (2475.3 – 2477 eV) is present, as well as a lesser S⁶⁺ peak
 744 and a minor sulfide peak (2465 – 2470 eV). Minimal S⁴⁺ beam damage ingrowth is observed
 745 with this diffuse beam analysis (compare to Figure 9). A sulfur-ionization peak (2483.5 – 2486
 746 eV) is present in S-XANES spectra of the both oxidized and reduced glasses. See Table 2 for
 747 identification of peaks and fit parameters. Reference peak position lines may vary slightly
 748 between samples depending on bond coordination environments.
 749

750 2.3.3 Correcting S-XANES beam damage

751 Since we include the S⁴⁺ peak in our fitting methodology, we can quantitatively separate
 752 the beam damage-induced S⁴⁺ signal from the overlapping broad S²⁻ peak in S-XANES spectra.
 753 This was not possible with the Jugo et al. (2010) method because all signal intensity over this
 754 region was considered as S²⁻, which would lead to spurious results in beam-damaged spectra
 755 (Figures 8, 9). During repeat measurements of hydrous, sulfur-rich, oxidized, anhydrite-saturated
 756 experimental basaltic glasses G466 and G479 (50 – 51 wt% SiO₂, 9000 – 15000 ppm S, 6.5 – 8.9
 757 wt% H₂O, 1300 – 1325 °C, 1.5 – 2.0 GPa; Table 1; Chowdhury and Dasgupta, 2019), we
 758 observe that progressive irradiation leads to increasing S⁴⁺ intensity and concomitant decreasing
 759 S⁶⁺ intensity (Figure 8) (Wilke et al., 2008; Métrich et al., 2009; Konecke et al., 2017). Because
 760 these glasses are highly oxidized, they contain no S²⁻ signal to overlap with the S⁴⁺ peak, which
 761 makes observation of the S⁴⁺ signal straightforward. As expected, increased photon doses with
 762 more focused beams cause more rapid S⁶⁺ to S⁴⁺ photo-reduction. Comparing the intensity ratio
 763 of S⁴⁺ peak ingrowth and S⁶⁺ peak loss during progressive beam damage from repeat
 764 measurements with photon flux densities ranging from 10⁶ to 10¹⁰ photons/s/μm², we find that
 765 S⁴⁺ peak ingrowth relates to S⁶⁺ intensity decrease by a factor of 1.2 ± 0.1 (1 SE; n = 7) (see
 766 **Data supplement**). We apply this scaling factor to observed S⁴⁺ peak intensities in beam
 767 damaged samples to restore original S⁶⁺ peak intensities via:

$$768 \quad \Sigma I[S^{6+}] = (I[S^{4+}] * F_{S^{4+/6+}}) + I[S^{6+}], [Eq. 2]$$

769 where $\Sigma I[S^{6+}]$ is the restored total S⁶⁺ S-XANES intensity, $I[S^{4+}]$ and $I[S^{6+}]$ are the measured
 770 Gaussian peak areas from S-XANES intensities, and $F_{S^{4+/6+}}$ is the S⁴⁺ to S⁶⁺ intensity scaling
 771 factor (1.2 ± 0.1; though this may be compositionally dependent, as discussed below). The ratio
 772 of S⁶⁺ signal intensity to total sulfur intensity is then:

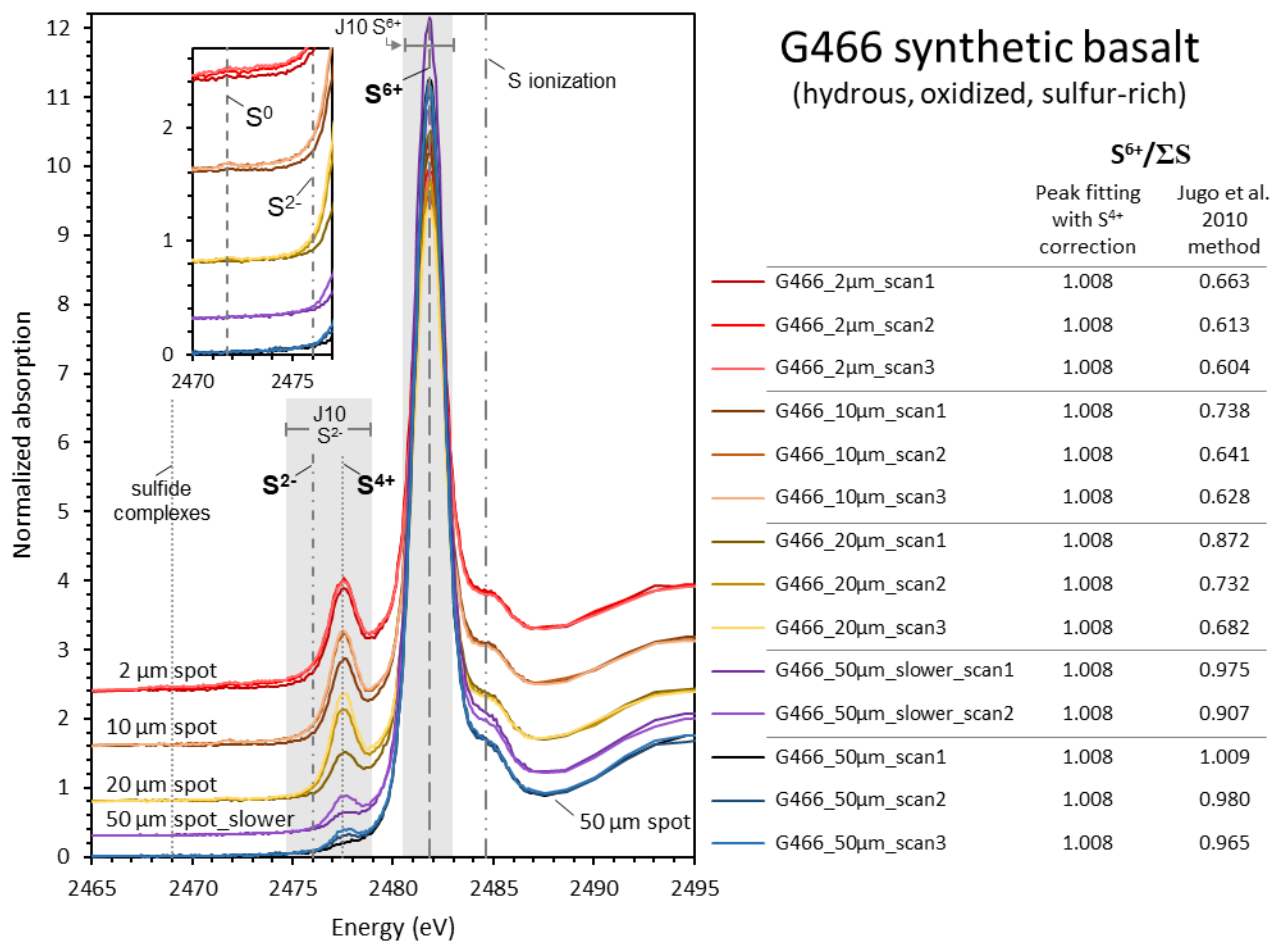
$$773 \quad I[S^{6+}] / \Sigma I[S^T] = \Sigma I[S^{6+}] / (I[S^{2-}] + \Sigma I[S^{6+}]), [Eq. 3]$$

774 Inputting this value into our peak fitting calibration based on the Jugo et al. (2010) glass suite
775 (Eq. 1) calculates the beam damage-restored sulfur speciation.

776 In addition to the obvious S⁴⁺ peak growth during beam damage of G466 and G479
777 glasses, we observe the ingrowth of a very small peak between 2471.6 – 2472.0 eV (Figure 8
778 inset), which is in the energy absorption range attributed to S⁰ (Fleet et al., 2005; Métrich et al.,
779 2009) or H₂S (Klimm et al., 2012a). This 2471.6 – 2472.0 eV peak is recognized during
780 successive analyses using 2×2, 10×10, and 20×20 μm spots (10¹⁰ to 10⁸ photons/s/μm²), but is a
781 negligible feature compared to the S⁴⁺ and S⁶⁺ signals. We also observe a slight absorption
782 increase in the broad energy range between 2470 – 2475 eV, which overlaps the S²⁻ glassy
783 absorption range. These subtle features are not included in our beam damage correction
784 approach, as peak-fitting such low-intensity features was inconsistent and sensitive to slight
785 variations in the spectra normalization routine. However, these additional features of S-XANES
786 beam damage invite future investigation.

787

788



789

790 **Figure 8.** Normalized spectra of oxidized, anhydrite-saturated, experimental glass G466 with
 791 repeat measurements in different locations with progressively greater photon flux densities
 792 (6.2×10^6 , 4.3×10^6 , 1.1×10^8 , 4.2×10^8 , and 1.1×10^{10} photons/s/ μm^2 for the 50 μm , 50 μm _slower,
 793 20 μm , 10 μm , and 2 μm scans, respectively). Spectra have been vertically shifted for clarity. The
 794 ingrowth of S^{4+} (2476.8 – 2477.7 eV) at the expense of S^{6+} (2480 – 2482.3 eV) is seen in repeat
 795 measurements at all spot sizes, and is increasingly pronounced with more focused beams. S^{4+}
 796 ingrowth stops after reaching a maximum intensity during the first focused $2 \times 2 \mu\text{m}$ spot analysis,
 797 with no further ingrowth during subsequent analyses. (*inset*) Detailed view of the 2470 – 2476
 798 eV region showing the ingrowth of a small peak at ~ 2471.7 eV and a slight absorption increase
 799 across 2470 – 2475 eV in analyses with focused beams. Each individual scan length was 5
 800 minutes, except for G466_50 μm _scans that were each 10 minutes. $S^{6+}/\Sigma S$ calculations using the
 801 peak fitting approach and correcting for S^{4+} photo-reduction are compared with $S^{6+}/\Sigma S$ calculated
 802 using the Jugo et al. (2010) method (“J10” gray S^{2-} and S^{6+} regions [energy shifted as
 803 discussed]), where the S^{4+} photo-reduction peak would be counted as part of the S^{2-} signal.
 804 Reference peak position lines may vary slightly between samples.

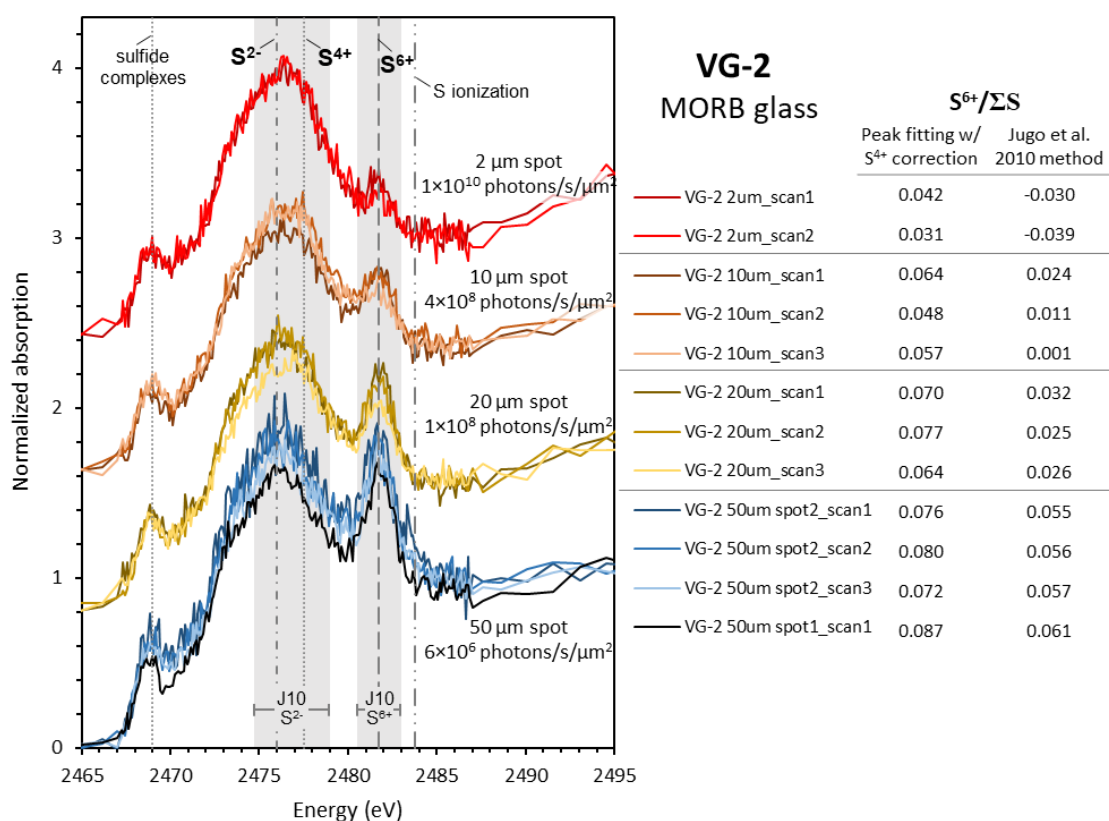
805

806 **2.3.4 Observations of natural glasses and melt inclusions**

807 We observe the same rapid S^{6+} to S^{4+} photo-reduction in numerous natural glasses.
808 Hydrous basaltic MI from the southern Cascades (up to 3.7 wt% H_2O) undergo rapid photo-
809 reduction (Muth and Wallace, 2021), which is consistent with hydrous basalts being highly
810 susceptible to speciation changes during X-ray irradiation (Cottrell et al., 2018; Moussallam et
811 al., 2019). However, we also observe rapid photo-reduction during S-XANES analyses of low-
812 H_2O tholeiitic basaltic glasses that have been observed to be very stable during Fe-XANES
813 analyses (Cottrell et al., 2009; Zhang et al., 2018). Repeated rapid S-XANES scans of the MORB
814 glass standard VG-2 (NMNH 111240-52; Juan de Fuca ridge) again show a marked decrease in
815 S^{6+} and ingrowth of S^{4+} during successive analyses (Figure 9). S-XANES measurements of VG-2
816 have been presented elsewhere (e.g., Head et al., 2018), but have typically been analyzed with a
817 more focused beam and longer measurement times than used here, which we observe to cause a
818 near complete conversion of S^{6+} to S^{4+} . VG-2 glass is relatively reduced ($0.15 Fe^{3+}/\Sigma Fe$, fayalite-
819 magnetite-quartz buffer [FMQ] +0.0; Zhang et al., 2018) so that the original S^{6+} is low and the
820 photo-reduction S^{4+} peak is correspondingly small. The small S^{4+} peak is therefore difficult to
821 discern from the dominant S^{2-} peak, which potentially explains why beam damage in VG-2 glass
822 has not been previously recognized. A North Pacific MORB glass analyzed via S-XANES with a
823 defocused beam by Métrich et al. (2009) also had a recognizable small S^{6+} peak, consistent with
824 our observations of VG-2. Applying our peak fitting and S^{4+} to S^{6+} correction approach to the
825 least beam-damaged VG-2 analyses ($50 \times 50 \mu m$ spot size; 1.1×10^7 photons/s/ μm^2 flux density),
826 we estimate that VG-2 MORB glass has $0.079 \pm 0.003 S^{6+}/\Sigma S$ (1 SE, $n = 4$). S-XANES
827 measurements of two additional MORB glasses, JDF-46N and ALV892-1 (Woods Hole
828 Oceanographic Institution, Northeast National Ion Microprobe Facility internal standards), at low
829 photon flux densities ($2 - 3 \times 10^7$ photons/s/ μm^2) give similar $S^{6+}/\Sigma S$ of 0.081 ± 0.001 and 0.093
830 ± 0.001 , respectively (1 SE, $n=4$ for each glass). Tests at higher photon flux densities ($10^8 - 10^{10}$
831 photons/s/ μm^2) or with long analysis durations (>6 minutes) show that JDF-46N and ALV892-1
832 also undergo rapid S^{6+} to S^{4+} photo-reduction (Figure 10), indicating a common susceptibility for
833 X-ray induced photo-reduction among low- H_2O MORB samples.

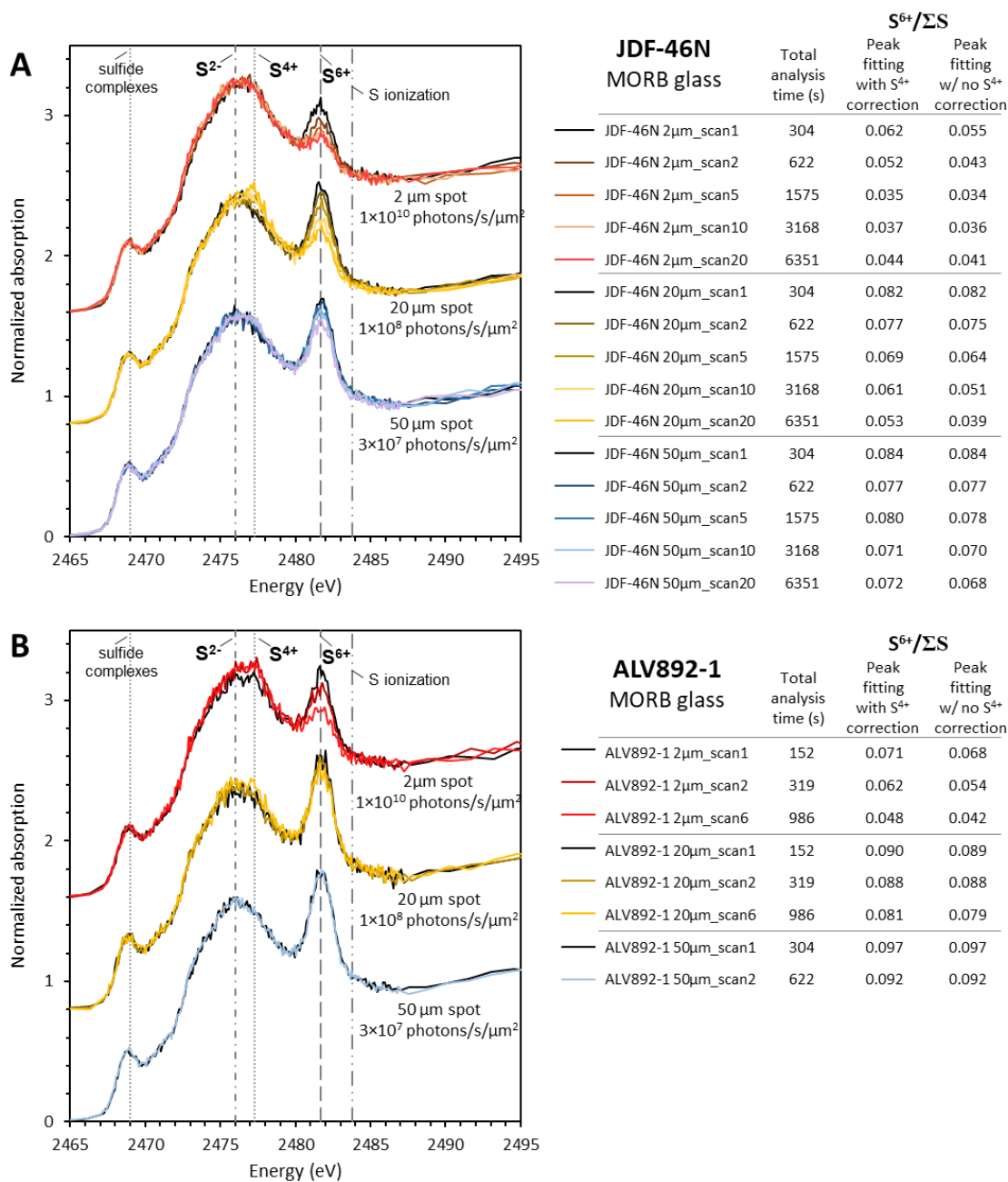
834 The measured $0.08 - 0.09 S^{6+}/\Sigma S$ in these three MORB samples are similar to the upper
835 end of the $0.03 - 0.07 S^{6+}/\Sigma S$ range measured in MORB glasses via EPMA S- $K\alpha$ wavelength
836 shift (Wallace and Carmichael, 1994) (although the EPMA-measured samples may have suffered

837 from electron beam-induced photo-oxidation [Jugo et al., 2010]). These measurements are all
 838 elevated compared to the 0.00 – 0.02 $S^{6+}/\Sigma S$ measured by S-XANES in four MORB glass
 839 samples by Jugo et al. (2010). Based on global MORB average fO_2 estimates of FMQ $-0.17 \pm$
 840 0.15 (0.014 ± 0.01 $Fe^{3+}/\Sigma Fe$) by Cottrell et al. (2020) or FMQ $+0.1$ by Berry et al. (2018), the
 841 Jugo et al. (2010) relationship of S^{6+} to fO_2 predicts that MORB glasses should contain almost
 842 exclusively sulfide (≤ 0.01 $S^{6+}/\Sigma S$). However, our observations indicate that MORB glasses are
 843 not universally sulfate-free and, at least in the three localities analyzed here, contain low but
 844 resolvable S^{6+} (up to 0.09 $S^{6+}/\Sigma S$).
 845



846
 847 **Figure 9.** Normalized S-XANES spectra of MORB glass standard VG-2 with repeat
 848 measurements in different locations using progressively greater photon flux densities (6.4×10^6 ,
 849 1.1×10^8 , 4.3×10^8 , 1.1×10^{10} photons/s/ μm^2 for the 50 μm , 20 μm , 10 μm , and 2 μm scans,
 850 respectively). Spectra have been vertically shifted for clarity. The ingrowth of S^{4+} (2476 –
 851 2477.7 eV) and loss of S^{6+} (2480.5 – 2483.3 eV) is increasingly apparent during analysis with
 852 more focused beams. Measurements with a fully focused 2 \times 2 μm beam cause the S^{6+} signal to be
 853 almost completely lost. Note the difficulty of recognizing the S^{4+} peak against the dominant S^{2-}
 854 broad peak at 2472 – 2480 eV, giving the illusion of a beam damage-free spectra. Each
 855 individual scan duration was 5 minutes. $S^{6+}/\Sigma S$ calculations using the peak fitting approach and
 856 correcting for S^{4+} photo-reduction are compared with $S^{6+}/\Sigma S$ calculated using the Jugo et al.

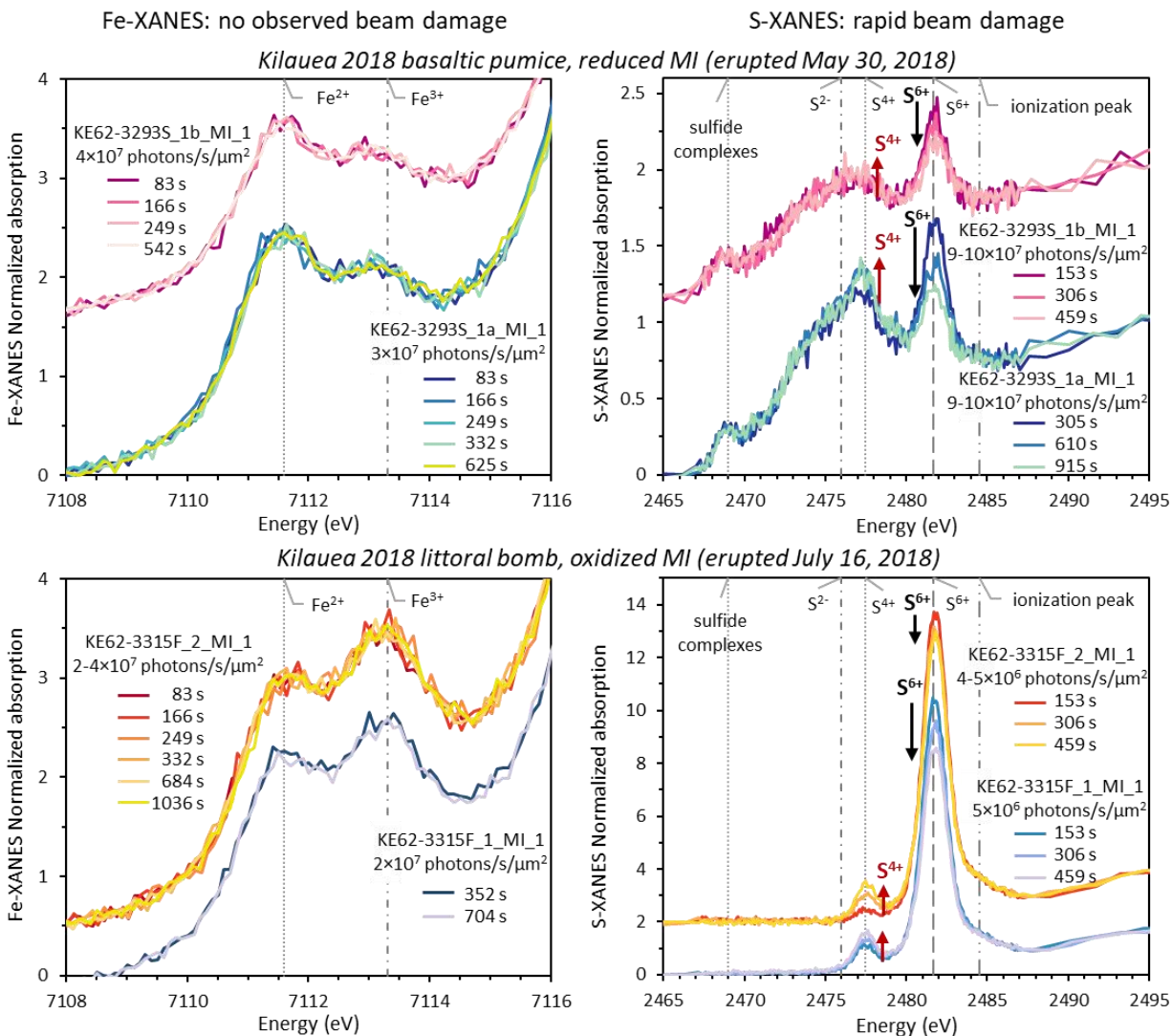
857 (2010) method (“J10” gray S²⁻ and S⁶⁺ regions [energy shifted as discussed]), where the S⁴⁺
 858 photo-reduction peak would be counted as part of the S²⁻ signal. Reference peak position lines
 859 may vary slightly between samples.
 860



861
 862 **Figure 10.** Normalized S-XANES spectra of MORB glasses JDF-46N and ALV892-1 with
 863 repeat measurements in different locations using progressively greater photon flux densities.
 864 Spectra have been vertically shifted for clarity. Spectra shown are examples from long sequences
 865 of repeated analyses (20 repeated scans for JDF-46N; 2 – 6 repeated scans for ALV892-1).
 866 Cumulative irradiation durations are listed on the right, and S⁶⁺/ΣS calculations using the peak
 867 fitting approach with and without correcting for S⁴⁺ photo-reduction are compared. As in Figure

868 9, the ingrowth of S^{4+} (2476 – 2477.7 eV) and loss of S^{6+} (2480.5 – 2483.3 eV) is increasingly
869 apparent during longer analyses and those with more focused beams. Note that S^{4+} corrections do
870 not reproduce the $S^{6+}/\Sigma S$ observed with low photon density measurements, indicating that
871 challenge of applying beam damage corrections in reduced glasses with overlapping S^{2-} and S^{4+}
872 peak areas. Reference peak position lines may vary slightly between samples.
873

874 We also observe S^{6+} to S^{4+} photo-reduction during S-XANES analyses of low- H_2O
875 basaltic MI samples from the 2018 lower East Rift Zone (LERZ) fissure eruption of Kīlauea
876 Volcano, HI (≤ 0.3 wt% H_2O [Lerner et al., in revision]). Depending on the degree of
877 atmospheric interaction prior to quenching, the Kīlauea olivine-hosted MI range from reduced to
878 highly oxidized (FMQ -0.7 to +2.4; Lerner, 2020). S-XANES beam damage occurs in Kīlauea
879 MI throughout this wide range of oxidation states (Figure 11). The S^{6+} to S^{4+} photo-reduction
880 during X-ray irradiation in Kīlauea MI and in MORB glasses is particularly interesting because
881 these low- H_2O ocean island basalt (OIB) and MORB glasses are stable during Fe-XANES
882 measurements (Figure 11), having Φ values ≤ 0.1 (Table 1). These observations highlight that
883 major (e.g., iron) and minor (e.g., sulfur) elements may have different susceptibilities to X-ray
884 induced beam damage (Gonçalves Ferreira et al., 2013). Alternatively or additionally, the
885 different responses of iron and sulfur during irradiation may be related to their behavior as non-
886 volatile and volatile elements, or to the ratio of redox couples (e.g., S/Fe concentration ratios)
887 (Hughes et al., 2020).
888



889

890 **Figure 11.** Four MI from the Kīlauea 2018 LERZ eruption were analyzed by both Fe- and S-
 891 XANES and exhibit differing susceptibilities to beam damage. Fe-XANES (*left*) and S-XANES
 892 (*right*) analyses were conducted in different locations within the same MI. Repeated rapid
 893 analyses were conducted for each technique, as described in the text, and the cumulative ending
 894 time in seconds (s) for successive scans are shown. Melt inclusions in both reduced, rapidly
 895 quenched basaltic pumice (KE62-3293S, *top*) and oxidized littoral bomb samples (KE62-3315F,
 896 *bottom*) exhibit no Fe²⁺ to Fe³⁺ photo-oxidation during repeat measurements, but the same MI
 897 undergo rapid S⁶⁺ to S⁴⁺ photo-reduction during S-XANES analyses. All MI contain ≤0.3 wt%
 898 H₂O and have Φ < 0.1. Spot sizes were 10×10 μm for Fe-XANES and 10×10 or 20×20 μm for S-
 899 XANES resulting in photon flux densities of 2 – 4×10⁷ and 4 – 10×10⁷ photons/s/μm² for Fe-
 900 and S-XANES measurements, respectively. Vertical lines are approximate reference peak
 901 positions, which may vary slightly between samples.
 902

903 **2.3.5 Discussion and summary**

904 The S-XANES peak fitting calibration and the determination of the S^{4+} to S^{6+} intensity
905 scaling factor could be improved with calibrations that include different compositions beyond the
906 basalts tested here (experimental glasses of Jugo et al. [2010] and Chowdhury and Dasgupta
907 [2019]). In particular, the concentration of Ca and Fe^{2+} may exert some control on sulfur
908 speciation at given fO_2 conditions and potentially on beam damage susceptibility in glasses (Graz
909 et al., 2007; Klimm et al., 2012a,b). H_2O -content may also play a role in S-XANES beam
910 damage susceptibility (Wilke et al., 2008) as it does in Fe-XANES photo-oxidation (Cottrell et
911 al., 2018). As an example, calculations of sulfur speciation in MORB glasses using the S^{4+} to S^{6+}
912 scaling factor of 1.2 to account for sulfur photo-reduction result in systematically lower $S^{6+}/\Sigma S$
913 for progressively more beam damaged analyses (from 0.09 to 0.03 $S^{6+}/\Sigma S$) (Figures 9, 10). This
914 indicates that the S^{4+} to S^{6+} scaling factor is likely larger for anhydrous, reduced basalt than what
915 we have determined for hydrous, oxidized basaltic glass. A S^{4+} to S^{6+} scaling factor of >3 is
916 required to equate the $S^{6+}/\Sigma S$ of highly beam damaged MORB analyses with the undamaged
917 measurements made using very low photon flux densities. However, we note that fitting the S^{4+}
918 peak is challenging in more reduced samples due to the overlap of the dominant S^{2-} peak with the
919 relatively minor S^{4+} peak, and we might be under-fitting the S^{4+} peak in the MORB spectra.
920 Additionally, in samples with mixed sulfur speciation, the slight beam damage-induced energy
921 increase in the 2470 – 2475 eV range (Figure 8 inset) would be completely masked by, and
922 included within, the broad S^{2-} peak area. Further characterizing the complete range of sulfur
923 complexing and valence changes during beam damage will be important for further improving S-
924 XANES correction methods. The uncertainties in the S^{4+} to S^{6+} intensity corrections underscore
925 that the foremost approach during S-XANES measurements should be to minimize beam damage
926 as much as possible, so that the overall uncertainties stemming from any S^{4+} corrections are
927 small.

928 In summary, S-XANES beam damage can occur in both hydrous and anhydrous silicate
929 glasses, but can be identified through repeat rapid scans by the presence and growth of a S^{4+}
930 peak. If beam damage is found to occur, we suggest focusing on the least damaged spectra for
931 each measurement, and then applying a S^{4+} to S^{6+} scaling factor to restore S^{4+} signal to the
932 original S^{6+} intensity. In high-sulfur samples, where signal intensity is sufficient even with rapid
933 scans, this is the ideal approach as beam damage is first limited and then restored to a good

934 approximation of original S^{6+} intensity. Low-sulfur samples may require merging multiple rapid
935 scans to obtain quantifiable spectra, despite the longer cumulative analysis time inducing more
936 photo-reduction. In long duration or merged scans, irradiation-induced S^{4+} signal can still be
937 restored to S^{6+} intensity, and although this introduces greater uncertainty (due to imprecisely
938 known S^{4+} to S^{6+} scaling factors), it is still a better approach than not applying any beam damage
939 correction. In highly oxidized samples lacking S^{2-} , accounting for S^{4+} is less important as it can
940 simply be assumed that all sulfur was originally present as S^{6+} . However, in samples with mixed
941 sulfur speciation, separating any S^{4+} photo-reduction signal from the overlapping S^{2-} peak, and
942 restoring the S^{4+} to original S^{6+} is important in accurately determining the initial sulfur speciation
943 of the glass.

944

945 **3.1 Identifying Fe-oxide nanolite crystals in Fe-XANES spectra**

946 In addition to beam damage concerns during XANES analyses of glasses, the possible
947 cryptic occurrence of nanolite crystals in glasses must also be considered to avoid spurious
948 interpretations of XANES spectra. Nanolites are minerals in the sub-micron range that are
949 typically undecipherable with optical microscopes or even with electron microscopes, but can
950 form in MI during quenching under certain conditions. In some settings, dispersed nanolite
951 crystals become large enough to appear as a fine “dust” within MI (Danyushevsky et al., 2002;
952 Wallace et al., 2003). It has been suggested that Fe-oxides and sulfides may form in MI during
953 cooling and/or diffusive H_2O -loss (Danyushevsky et al., 2002; Rowe et al., 2007; Di Genova et
954 al., 2017, 2018; Head et al., 2018). Di Genova et al. (2017, 2018) observe that Fe-oxide
955 (magnetite) nanolites preferentially occur in H_2O -rich glasses (≥ 2.5 wt% H_2O) across a range of
956 compositions, suggesting that high H_2O promotes nanolite formation during quenching. This
957 might occur, for example, because increased H_2O lowers the glass transition temperature,
958 resulting in a larger cooling interval in the liquid state for H_2O -rich melts (Deubener et al.,
959 2003). The presence of nanolites complicates XANES, Raman, and EPMA redox measurements
960 in glasses because the bonding coordination in nanolite minerals may lead to different
961 relationships between ion abundances and signal intensities compared to calibrated relationships
962 in glasses.

963 Fortunately, the short-range ordering of iron and sulfur in mineral phases can be readily
964 detected via XANES and Raman spectral techniques (Wilke et al., 2006; Di Genova et al., 2017,
965 2018; Head et al., 2018). Magnetite nanolites have been spectrally identified by Raman
966 measurements in MI from basalts, dacites, and trachytes containing >4.5 wt% FeO^{T} and ≥ 2.5
967 wt% H_2O (Di Genova et al., 2017, 2018). Magnetite nanolite abundance correlates with more
968 oxidized (EPMA-calculated) redox states of MI (Hughes et al., 2018), although it is unclear if
969 nanolites actually form in more oxidized MI, or rather that the presence of nanolites affects the
970 redox quantification. Ni-, V-, and S-XANES have been used by Farges et al. (2001) to identify
971 Ni-bearing nanolites in hydrous albitic experimental glasses (≥ 4.5 wt% H_2O) and by Head et al.
972 (2018) to identify V- and S-bearing spinel and sulfide nanolites in natural basaltic MI from
973 Nyamuragira volcano (D.R. Congo). Finally, Fe-XANES has been used by Wilke et al. (2006) to
974 identify the formation of Fe-oxide nanolites during the slow quenching of hydrous haplogranitic
975 experimental glasses (where $0.06 - 1.5$ μm diameter maghemite nanolites were confirmed by
976 TEM).

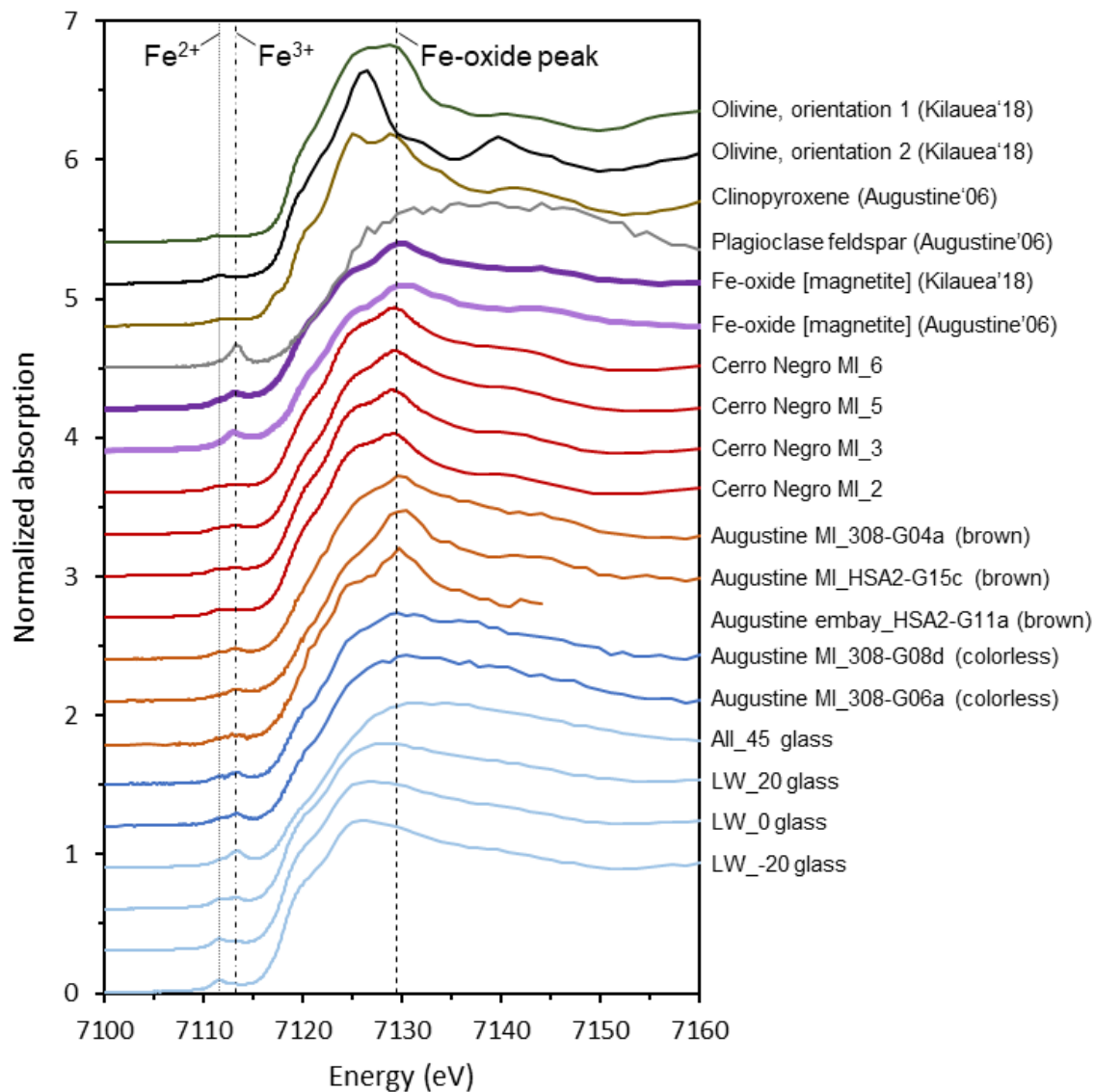
977 Here, we build on the observations of Wilke et al. (2006) and show that Fe-XANES
978 measurements can identify the cryptic occurrence of Fe-oxide nanolites in naturally quenched,
979 optically glassy MI. We conducted Fe-XANES measurements of doubly-intersected dacitic-
980 rhyolitic MI from the 2006 eruption of Augustine Volcano (AK, USA) (Lerner, 2020) and of
981 basaltic MI from Cerro Negro (Nicaragua) (Gaetani et al., 2012). A number of these MI contain
982 a sharp absorption peak at ~ 7129.5 eV that is similar to the absorption edge feature observed in
983 magnetite phenocrysts from both Augustine and oxidized Kīlauea 2018 LERZ samples (Figure
984 12). This magnetite-like peak indicates increased crystalline ordering of iron in the glasses due to
985 Fe-oxide nanolites (Wilke et al., 2006). A magnetite-like peak was also observed in Fe-XANES
986 measurements of optically glassy quartz-hosted MI from Central Andean volcanic centers by
987 Grocke et al. (2016), who similarly considered this feature to indicate Fe-oxide nanolite
988 interference.

989 Melt inclusions in Augustine feldspar and pyroxene grains that contain Fe-oxide
990 (presumably magnetite or maghemite) nanolites are consistently a brown color, although no
991 distinct fine-scale crystals are observable with either optical or electron microscopes (Figures 12,
992 13). Optically colorless MI are also present in the same samples from Augustine, and these
993 colorless MI have smooth Fe-XANES absorption edge spectra that are indicative of glass with no

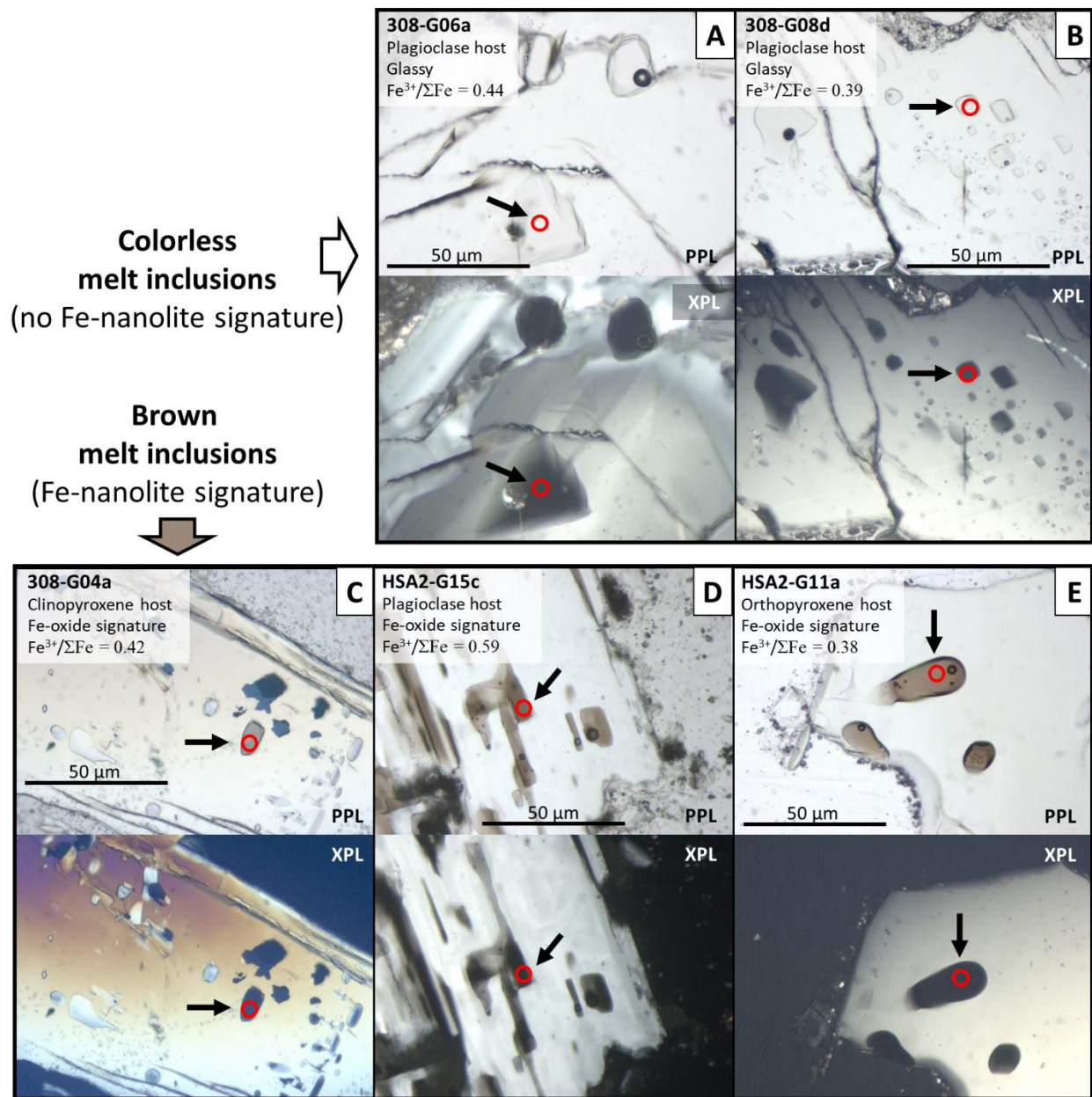
994 magnetite-like structure (Figures 12, 13). The occurrence of colorless and brown MI, even within
995 the same sample, has been long recognized, and the cause and importance of MI glass color has
996 been much debated. Although some studies have found that colorless MI contain lower H₂O and
997 higher CO₂ than co-occurring brown MI, other studies find negligible differences in volatiles or
998 major element compositions between different colored MI (Wallace et al., 1999; Myers et al.,
999 2016; Myers, 2017). However, Fe-XANES analyses show that the color of Augustine MI
1000 consistently reflects the presence or absence of magnetite nanolites. These findings are consistent
1001 with observations of Fe-oxide (and other crystalline phases) nanolites causing the dark color of
1002 natural obsidian and rhyolitic glass (e.g., Sharp et al., 1996; Castro et al., 2005; Ma et al., 2007;
1003 Tuffen et al., 2021; Galois and Calas, 2021). Iron nanolite-bearing Augustine MI have highly
1004 variable calculated Fe³⁺/ΣFe, but in general, these MI are more Fe³⁺-rich compared to colorless,
1005 nanolite-free MI from the same tephra sample (Lerner, 2020). However, it is again unclear
1006 whether this observation reflects an increased oxidation state within the nanolite-bearing MI or if
1007 it is a consequence of greater Fe³⁺ signal from the crystalline nanolite phases. Importantly, the
1008 presence of Fe-oxide nanolites may invalidate the Fe-XANES centroid energy to Fe³⁺/ΣFe
1009 calibrations for glasses. Until further research is undertaken to investigate such effects on
1010 XANES calibrations, spectra containing nanolite signatures should be interpreted cautiously. To
1011 help focus sample selection and avoid nanolite-induced complications during synchrotron
1012 analyses, Raman spectra could be acquired prior to XANES analyses to identify whether
1013 nanolites are present in target glasses (Di Genova et al., 2017, 2018).

1014 We note that many brown-colored MI in more basaltic compositions have clean glassy
1015 XANES spectra with no evidence of nanolites (e.g., many Kīlauea LERZ and southern Cascades
1016 olivine-hosted MI studied here), so MI color alone does not always indicate the presence of Fe-
1017 oxide nanolites. Future efforts to characterize compositional, temperature, and H₂O variations
1018 between co-occurring brown and colorless MI in the same units will better clarify the processes
1019 that govern Fe-oxide nanolite formation and MI glass color.

1020



1021
 1022 **Figure 12.** Normalized Fe-XANES spectra of mineral spectra (olivine, clinopyroxene, feldspar,
 1023 magnetite), reference glasses (LW series, All_45; Cottrell et al., 2009), and doubly-intersected
 1024 MI or melt embayment glasses from Augustine 2006 (samples shown in Figure 13) and Cerro
 1025 Negro (see **Data supplement**). Brown-colored dacitic-rhyolitic glasses from Augustine (orange
 1026 lines) have a prominent peak at ~7129.5 eV that closely resemble magnetite spectra (thick purple
 1027 lines), indicating the presence of Fe-oxide nanolites. Cerro Negro olivine-hosted basaltic MI (red
 1028 lines) also have a 7129.5 eV signature of magnetite nanolites. Colorless MI from Augustine (blue
 1029 lines) have glassy spectra, similar to oxidized reference glasses LW_20 and All_45 (FMQ +2
 1030 and +4.5, respectively). Spectra have been vertically shifted for clarity. The lines labeled Fe²⁺
 1031 and Fe³⁺ refer to the approximate peak positions of the first and second pre-edge doublet.
 1032
 1033
 1034



1035
1036 **Figure 13.** Doubly-intersected dacitic-rhyolitic MI (A, B, C, D) and melt embayments (E)
1037 erupted from Augustine in 2006. (top) Colorless glasses (A, B) and (bottom) brown glasses with
1038 Fe-oxide nanolite spectral signatures (C, D, E) are present in inclusions and embayments within
1039 plagioclase (A, B, D, E) and pyroxene (C). Each two-pane panel shows images with plane
1040 polarized light (PPL) and through crossed polarizers (XPL), with full glass extinction in XPL
1041 showing where MI are doubly-intersected for host-free Fe-XANES analysis. All Fe-XANES
1042 analyses were conducted with a $5 \times 5 \mu m$ spot size ($\sim 1.4 \times 10^8$ photons/s/ μm^2 flux densities), and
1043 spectra are shown in Figure 12. Photo-oxidation was not observed during repeated analyses in
1044 these glasses. $Fe^{3+}/\Sigma Fe$ was calculated from the felsic glass calibration of Fiege et al. (2017),
1045 although we note that the presence of Fe-oxide nanolites in the brown MI may invalidate such
1046 $Fe^{3+}/\Sigma Fe$ calculations.

1047

1048

1049 **4.1 Conclusions and implications**

1050 Accurate XANES measurements are essential for inferring magma redox state from iron
1051 and sulfur valence states in quenched glasses. Using repeated, rapid Fe- and S-XANES
1052 measurements and implementing a new peak-fitting calibration for S-XANES, we have
1053 developed time-dependent corrections to identify and correct for beam damage during Fe- and S-
1054 XANES analyses of silicate glasses. Beam damage corrections for iron photo-oxidation and
1055 sulfur photo-reduction are determined for each individual analysis rather than applying
1056 generalized corrections. This allows versatility to account for composition differences and the
1057 effects of variable H₂O concentrations in MI that are commonly found in an individual tephra
1058 sample, which can influence beam damage susceptibility. Testing these beam damage correction
1059 methods on hydrous experimental basalts, we show that Fe- and S-XANES measurements can be
1060 reliably made even on beam-sensitive glasses. Additional studies of the mechanisms and
1061 compositional dependence of S-XANES beam damage could further improve the photo-
1062 reduction correction method that we have introduced here. Additionally, using Fe-XANES, we
1063 demonstrate the occurrence of cryptic Fe-oxide nanolites in naturally quenched MI. Melt
1064 inclusions containing nanolite phases may invalidate Fe- and S-XANES calibrations for
1065 elemental valence and speciation in glasses, and such spectra should be interpreted with caution.

1066 The analytical techniques presented here extend the ability to reliably measure iron
1067 valence and sulfur speciation in small and/or hydrous MI, which can undergo substantial beam
1068 damage during XANES analyses. These methods will allow further exploration of the redox
1069 behavior in hydrous systems, such as magmatic arcs and high-H₂O intraplate volcanic settings.
1070 Measurements of redox conditions in magmatic arc glasses are of particular interest to assess
1071 whether subduction inputs oxidize the sub-arc mantle and the relative importance of fO_2 in
1072 controlling volcanic degassing and the formation of porphyry copper ore deposits.

1073 We demonstrate that irradiation-induced changes in S-XANES spectra occur rapidly even
1074 in H₂O-poor MORB and OIB glasses that do not experience beam damage during Fe-XANES
1075 analysis. This raises the possibility that other multivalent trace element may similarly be subject
1076 to variation during X-ray analysis, even in relatively anhydrous glasses. The time-dependent
1077 analytical techniques presented here can be extended to XANES analyses of other multivalent

1078 trace elements, which are being increasingly applied to volcanic glasses (e.g., V-, Cr-, Cu-
1079 XANES; Sutton et al., 2020), to assess whether changes in valence or molecular complexing
1080 may be occurring during irradiation.

1081

1082 **Acknowledgements**

1083 This manuscript was significantly improved thanks to constructive input from journal
1084 reviewers and editors. We thank D. Johnston and J. Watkins (University of Oregon), the U.S.
1085 Geological Survey's Hawaiian Volcano Observatory, and the Smithsonian Institution's
1086 Department of Mineral Sciences for access to some of the samples analyzed in this study. We
1087 also thank J. Donovan and J. Chouinard (University of Oregon) for EPMA assistance. This
1088 research used resources of the Advanced Photon Source, a U.S. Department of Energy (DOE)
1089 Office of Science User Facility operated for the DOE Office of Science by Argonne National
1090 Laboratory under Contract No. DE-AC02-06CH11357. We acknowledge the support of
1091 GeoSoilEnviroCARS at the Advanced Photon Source, which is supported by NSF - Earth
1092 Sciences (EAR-1128799), and the Department of Energy, Geosciences (DE-FG02-94ER14466).
1093 A.H.L and M.J.M. acknowledge support from the National Science Foundation Graduate
1094 Research Fellowship Program (NSF-GRFP) under grant 1309047 and internships provided
1095 through the Graduate Research Internship Program (GRIP). P.J.W. acknowledges funding
1096 support from the National Science Foundation under grant EAR-1834959. Any findings and
1097 conclusions or recommendations expressed in this material are those of the authors and do not
1098 necessarily reflect the views of the National Science Foundation.

1099

1100 **Author Contributions**

1101 A.H.L. and M.J.M. conceived of the project and led sample preparation, analysis, data
1102 synthesis, and authoring. P.J.W., A.L., and M.N. aided in project design, data interpretation, and
1103 manuscript editing. G.A.G., P.C., and R.D. aided in sample preparation and manuscript editing.

1104 **References**

- 1105 Anzures B. A., Parman S. W., Milliken R. E., Lanzirotti A. and Newville M. (2020) XANES
1106 spectroscopy of sulfides stable under reducing conditions. *American Mineralogist* **105**,
1107 375–381.
- 1108 Backnaes L., Stelling J., Behrens H., Goettlicher J., Mangold S., Verheijen O., Beerkens R. G. C.
1109 and Deubener J. (2008) Dissolution Mechanisms of Tetravalent Sulphur in Silicate Melts:
1110 Evidences from Sulphur K Edge XANES Studies on Glasses. *Journal of the American*
1111 *Ceramic Society* **91**, 721–727.
- 1112 Bajt S., Sutton S. R. and Delaney J. S. (1994) X-ray microprobe analysis of iron oxidation states
1113 in silicates and oxides using X-ray absorption near edge structure (XANES). *Geochimica*
1114 *et Cosmochimica Acta* **58**, 5209–5214.
- 1115 Baker D. R. and Moretti R. (2011) Modeling the solubility of sulfur in magmas: a 50-year old
1116 geochemical challenge. *Reviews in Mineralogy and Geochemistry* **73**, 167–213.
- 1117 Barnes J. D., Prather T. J., Cisneros M., Befus K., Gardner J. E. and Larson T. E. (2014) Stable
1118 chlorine isotope behavior during volcanic degassing of H₂O and CO₂ at Mono Craters,
1119 CA. *Bulletin of Volcanology* **76**, 805.
- 1120 Berry A. J., Danyushevsky L. V., O'Neill H. S. C., Newville M. and Sutton S. R. (2008)
1121 Oxidation state of iron in komatiitic melt inclusions indicates hot Archaean mantle.
1122 *Nature* **455**, 960.
- 1123 Berry A. J., O'Neill H. S. C., Jayasuriya K. D., Campbell S. J. and Foran G. J. (2003) XANES
1124 calibrations for the oxidation state of iron in a silicate glass. *American Mineralogist* **88**,
1125 967–977.
- 1126 Berry A. J., Stewart G. A., O'Neill H. S. C., Mallmann G. and Mosselmans J. F. W. (2018) A re-
1127 assessment of the oxidation state of iron in MORB glasses. *Earth and Planetary Science*
1128 *Letters* **483**, 114–123.
- 1129 Bonnin-Mosbah M., Métrich N., Susini J., Salomé M., Massare D. and Menez B. (2002) Micro
1130 X-ray absorption near edge structure at the sulfur and iron K-edges in natural silicate
1131 glasses. *Spectrochimica Acta Part B: Atomic Spectroscopy* **57**, 711–725.
- 1132 Bonnin-Mosbah M., Simionovici A. S., Métrich N., Duraud J.-P., Massare D. and Dillmann P.
1133 (2001) Iron oxidation states in silicate glass fragments and glass inclusions with a
1134 XANES micro-probe. *Journal of Non-Crystalline Solids* **288**, 103–113.
- 1135 Borisov A., Behrens H. and Holtz F. (2018) Ferric/ferrous ratio in silicate melts: A new model
1136 for 1 atm data with special emphasis on the effects of melt composition. *Contributions to*
1137 *Mineralogy and Petrology* **173**, 98.

- 1138 Botcharnikov R. E., Linnen R. L., Wilke M., Holtz F., Jugo P. J. and Berndt J. (2011) High gold
1139 concentrations in sulphide-bearing magma under oxidizing conditions. *Nature Geosci* **4**,
1140 112–115.
- 1141 Brounce M. N., Boyce J., McCubbin F. M., Humphreys J., Reppart J., Stolper E. and Eiler J.
1142 (2019) The oxidation state of sulfur in lunar apatite. *American Mineralogist* **104**, 307–
1143 312.
- 1144 Brounce M. N., Kelley K. A. and Cottrell E. (2014) Variations in $\text{Fe}^{3+}/\Sigma\text{Fe}$ of Mariana Arc
1145 basalts and mantle wedge $f\text{O}_2$. *Journal of Petrology* **55**, 2513–2536.
- 1146 Brounce M. N., Stolper E. and Eiler J. (2017) Redox variations in Mauna Kea lavas, the oxygen
1147 fugacity of the Hawaiian plume, and the role of volcanic gases in Earth's oxygenation.
1148 *Proceedings of the National Academy of Sciences* **114**, 8997–9002.
- 1149 Browaeys J. (2021) *Linear fit with both uncertainties in x and in y.*, MATLAB Central File
1150 Exchange.
- 1151 Callegaro S., Geraki K., Marzoli A., Min A. D., Maneta V. and Baker D. R. (2020) The quintet
1152 completed: The partitioning of sulfur between nominally volatile-free minerals and
1153 silicate melts. *American Mineralogist* **105**, 697–707.
- 1154 Carroll M. and Rutherford M. J. (1988) Sulfur speciation in hydrous experimental glasses of
1155 varying oxidation state—results from measured wavelength shifts of sulfur X-rays.
1156 *American Mineralogist* **73**, 845–9.
- 1157 Castro J. M., Dingwell D. B., Nichols A. R. and Gardner J. E. (2005) New insights on the origin
1158 of flow bands in obsidian. In *Kinematics and dynamics of lava flows* (eds. M. Manga and
1159 G. Ventura). Special Papers-Geological Society of America. Boulder, Colo.; Geological
1160 Society of America; 1999. pp. 55–65.
- 1161 Chowdhury P. and Dasgupta R. (2019) Effect of sulfate on the basaltic liquidus and Sulfur
1162 Concentration at Anhydrite Saturation (SCAS) of hydrous basalts—Implications for sulfur
1163 cycle in subduction zones. *Chemical Geology* **522**, 162–174.
- 1164 Cottrell E., Birner S., Brounce M. N., Davis F. A., Waters L. E. and Kelley K. A. (2020) Oxygen
1165 Fugacity Across Tectonic Settings. In *Redox variables and mechanisms in magmatism
1166 and volcanism* (eds. D. R. Neuville and R. Moretti). AGU Geophysical Monograph.
1167 Wiley.
- 1168 Cottrell E. and Kelley K. A. (2011) The oxidation state of Fe in MORB glasses and the oxygen
1169 fugacity of the upper mantle. *Earth and Planetary Science Letters* **305**, 270–282.
- 1170 Cottrell E., Kelley K. A., Lanzirotti A. and Fischer R. A. (2009) High-precision determination of
1171 iron oxidation state in silicate glasses using XANES. *Chemical Geology* **268**, 167–179.

- 1172 Cottrell E., Lanzirotti A., Mysen B., Birner S., Kelley K. A., Botcharnikov R., Davis F. A. and
1173 Newville M. (2018) A Mössbauer-based XANES calibration for hydrous basalt glasses
1174 reveals radiation-induced oxidation of Fe. *American Mineralogist* **103**, 489–501.
- 1175 Danyushevsky L. V., McNeill A. W. and Sobolev A. V. (2002) Experimental and petrological
1176 studies of melt inclusions in phenocrysts from mantle-derived magmas: An overview of
1177 techniques, advantages and complications. *Chemical Geology* **183**, 5–24.
- 1178 Dauphas N., Roskosz M., Alp E. E., Neuville D. R., Hu M. Y., Sio C. K., Tissot F. L. H., Zhao
1179 J., Tissandier L. and Médard E. (2014) Magma redox and structural controls on iron
1180 isotope variations in Earth’s mantle and crust. *Earth and Planetary Science Letters* **398**,
1181 127–140.
- 1182 Deubener J., Müller R., Behrens H. and Heide G. (2003) Water and the glass transition
1183 temperature of silicate melts. *Journal of Non-Crystalline Solids* **330**, 268–273.
- 1184 Di Genova D., Caracciolo A. and Kolzenburg S. (2018) Measuring the degree of “nanotilization”
1185 of volcanic glasses: Understanding syn-eruptive processes recorded in melt inclusions.
1186 *Lithos* **318**, 209–218.
- 1187 Di Genova D., Sicola S., Romano C., Vona A., Fanara S. and Spina L. (2017) Effect of iron and
1188 nanolites on Raman spectra of volcanic glasses: A reassessment of existing strategies to
1189 estimate the water content. *Chemical Geology* **475**, 76–86.
- 1190 Dyar M. D., McCanta M., Breves E., Carey C. J. and Lanzirotti A. (2016) Accurate predictions
1191 of iron redox state in silicate glasses: A multivariate approach using X-ray absorption
1192 spectroscopy. *American Mineralogist* **101**, 744–747.
- 1193 Elam W. T., Ravel B. D. and Sieber J. R. (2002) A new atomic database for X-ray spectroscopic
1194 calculations. *Radiation Physics and Chemistry* **63**, 121–128.
- 1195 Farges F., Lefrère Y., Rossano S., Berthereau A., Calas G. and Brown G. E. (2004) The effect of
1196 redox state on the local structural environment of iron in silicate glasses: a combined
1197 XAFS spectroscopy, molecular dynamics, and bond valence study. *Journal of Non-
1198 Crystalline Solids* **344**, 176–188.
- 1199 Farges F., Munoz M., Siewert R., Malavergne V., Brown G. E., Behrens H., Nowak M. and Petit
1200 P.-E. (2001) Transition elements in water-bearing silicate glasses/melts. part II. Ni in
1201 water-bearing glasses. *Geochimica et Cosmochimica Acta* **65**, 1679–1693.
- 1202 Fiege A., Holtz F., Shimizu N., Mandeville C. W., Behrens H. and Knipping J. L. (2014) Sulfur
1203 isotope fractionation between fluid and andesitic melt: An experimental study.
1204 *Geochimica et Cosmochimica Acta* **142**, 501–521.
- 1205 Fiege A., Ruprecht P., Simon A. C., Bell A. S., Göttlicher J., Newville M., Lanzirotti T. and
1206 Moore G. (2017) Calibration of Fe XANES for high-precision determination of Fe
1207 oxidation state in glasses: Comparison of new and existing results obtained at different
1208 synchrotron radiation sources. *American Mineralogist* **102**, 369–380.

- 1209 Fleet M. E., Liu X., Harmer S. L. and King P. L. (2005) Sulfur K-edge XANES spectroscopy:
1210 Chemical state and content of sulfur in silicate glasses. *The Canadian Mineralogist* **43**,
1211 1605–1618.
- 1212 Gaborieau M., Laubier M., Bolfan-Casanova N., McCammon C. A., Vantelon D., Chumakov A.
1213 I., Schiavi F., Neuville D. R. and Venugopal S. (2020) Determination of $\text{Fe}^{3+}/\Sigma\text{Fe}$ of
1214 olivine-hosted melt inclusions using Mössbauer and XANES spectroscopy. *Chemical*
1215 *Geology* **547**, 119646.
- 1216 Gaetani G. A., O’Leary J. A., Shimizu N., Bucholz C. E. and Newville M. (2012) Rapid
1217 reequilibration of H_2O and oxygen fugacity in olivine-hosted melt inclusions. *Geology*
1218 **40**, 915–918.
- 1219 Galois L. and Calas G. (2021) The unique speciation of iron in calc-alkaline obsidians.
1220 *Chemical Geology* **559**, 119925.
- 1221 Galois L., Calas G. and Arrio M. A. (2001) High-resolution XANES spectra of iron in minerals
1222 and glasses: structural information from the pre-edge region. *Chemical geology* **174**,
1223 307–319.
- 1224 Gonçalves Ferreira P., de Ligny D., Lazzari O., Jean A., Gonzalez O. C. and Neuville D. R.
1225 (2013) Photoreduction of iron by a synchrotron X-ray beam in low iron content soda-lime
1226 silicate glasses. *Chemical Geology* **346**, 106–112.
- 1227 Graz Y., Scaillet B., Pichavant M. and Gaillard F. (2007) The effect of sulfur on the $\text{Fe}^{2+}/\text{Fe}^{3+}$
1228 ratio of MORB and its implications for the redox state of the mantle.
- 1229 Grocke S. B., Cottrell E., de Silva S. and Kelley K. A. (2016) The role of crustal and eruptive
1230 processes versus source variations in controlling the oxidation state of iron in Central
1231 Andean magmas. *Earth and Planetary Science Letters* **440**, 92–104.
- 1232 Head E., Lanzirotti A., Newville M. and Sutton S. (2018) Vanadium, sulfur, and iron valences in
1233 melt inclusions as a window into magmatic processes: A case study at Nyamuragira
1234 volcano, Africa. *Geochimica et Cosmochimica Acta* **226**, 149–173.
- 1235 Helz R. T., Cottrell E., Brounce M. N. and Kelley K. A. (2017) Olivine-melt relationships and
1236 syneruptive redox variations in the 1959 eruption of Kīlauea Volcano as revealed by
1237 XANES. *Journal of Volcanology and Geothermal Research* **333**, 1–14.
- 1238 Hughes E. C., Buse B., Kearns S. L., Blundy J. D., Kilgour G., Mader H. M., Brooker R. A.,
1239 Balzer R., Botcharnikov R. E. and Di Genova D. (2018) High spatial resolution analysis
1240 of the iron oxidation state in silicate glasses using the electron probe. *American*
1241 *Mineralogist: Journal of Earth and Planetary Materials* **103**, 1473–1486.
- 1242 Hughes E. C., Buse B., Kearns S. L., Brooker R. A., Di Genova D., Kilgour G., Mader H. M. and
1243 Blundy J. D. (2020) The microanalysis of iron and sulphur oxidation states in silicate
1244 glass-Understanding the effects of beam damage. In *IOP Conference Series: Materials*
1245 *Science and Engineering* IOP Publishing. p. 012014.

- 1246 Jarosewich E., Nelen J. A. and Norberg J. A. (1980) Reference samples for electron microprobe
1247 analysis. *Geostandards Newsletter* **4**, 43–47.
- 1248 Jégo S. and Dasgupta R. (2014) The fate of sulfur during fluid-present melting of subducting
1249 basaltic crust at variable oxygen fugacity. *Journal of Petrology* **55**, 1019–1050.
- 1250 Jugo P. J. (2009) Sulfur content at sulfide saturation in oxidized magmas. *Geology* **37**, 415–418.
- 1251 Jugo P. J., Wilke M. and Botcharnikov R. E. (2010) Sulfur K-edge XANES analysis of natural
1252 and synthetic basaltic glasses: Implications for S speciation and S content as function of
1253 oxygen fugacity. *Geochimica et Cosmochimica Acta* **74**, 5926–5938.
- 1254 Kelley K. A. and Cottrell E. (2012) The influence of magmatic differentiation on the oxidation
1255 state of Fe in a basaltic arc magma. *Earth and Planetary Science Letters* **329–330**, 109–
1256 121.
- 1257 Kelley K. A. and Cottrell E. (2009) Water and the oxidation state of subduction zone magmas.
1258 *Science* **325**, 605–607.
- 1259 Kent A. J. (2008) Melt inclusions in basaltic and related volcanic rocks. *Reviews in Mineralogy
1260 and Geochemistry* **69**, 273–331.
- 1261 Klimm K., Kohn S. C. and Botcharnikov R. E. (2012a) The dissolution mechanism of sulphur in
1262 hydrous silicate melts. II: Solubility and speciation of sulphur in hydrous silicate melts as
1263 a function of fO_2 . *Chemical Geology* **322**, 250–267.
- 1264 Klimm K., Kohn S. C., O’Dell L. A., Botcharnikov R. E. and Smith M. E. (2012b) The
1265 dissolution mechanism of sulphur in hydrous silicate melts. I: Assessment of analytical
1266 techniques in determining the sulphur speciation in iron-free to iron-poor glasses.
1267 *Chemical Geology* **322**, 237–249.
- 1268 Konecke B. A., Fiege A., Simon A. C., Parat F. and Stechern A. (2017) Co-variability of S^{6+} ,
1269 S^{4+} , and S^{2-} in apatite as a function of oxidation state: Implications for a new
1270 oxybarometer. *American Mineralogist* **102**, 548–557.
- 1271 Kraft S., Stümpel J., Becker P. and Kuetgens U. (1996) High resolution x-ray absorption
1272 spectroscopy with absolute energy calibration for the determination of absorption edge
1273 energies. *Review of Scientific Instruments* **67**, 681–687.
- 1274 Kress V. C. and Carmichael I. S. (1991) The compressibility of silicate liquids containing Fe_2O_3
1275 and the effect of composition, temperature, oxygen fugacity and pressure on their redox
1276 states. *Contributions to Mineralogy and Petrology* **108**, 82–92.
- 1277 Kuehn S. C., Froese D. G., Shane P. A. R. and INTAV Intercomparison Participants (2011) The
1278 INTAV intercomparison of electron-beam microanalysis of glass by tephrochronology
1279 laboratories: results and recommendations. *Quaternary International* **246**, 19–47.

- 1280 Lanzirotti A., Lee L., Head E., Sutton S. R., Newville M., McCanta M., Lerner A. H. and
1281 Wallace P. J. (2019) Direct measurements of copper speciation in basaltic glasses:
1282 understanding the relative roles of sulfur and oxygen in copper complexation in melts.
1283 *Geochimica et Cosmochimica Acta* **267**, 164–178.
- 1284 Lerner A. H. (2020) The depths and locations of magma reservoirs and their consequences for
1285 the behavior of sulfur and volcanic degassing. Ph.D. Thesis, University of Oregon.
- 1286 Lerner A. H., Wallace P. J., Shea T., Mourey A. J., Kelly P. J., Nadeau P. A., Elias T., Kern C.,
1287 Clor L. E., Gansecki C., Lee R. L., Moore L. R. and Werner C. A. (2021) The petrologic
1288 and degassing behavior of sulfur and other magmatic volatiles from the 2018 eruption of
1289 Kīlauea, Hawai‘i: melt concentrations, magma storage depths, and magma recycling. *Bull*
1290 *Volcanol* **83**, 43.
- 1291 Li D., Bancroft G. M., Kasrai M., Fleet M. E., Feng X. and Tan K. (1995) S K- and L-edge X-
1292 ray absorption spectroscopy of metal sulfides and sulfates; applications in mineralogy
1293 and geochemistry. *The Canadian Mineralogist* **33**, 949–960.
- 1294 Ma C., Rossman G. R. and Miller J. A. (2007) The Origin of Color in “Fire” Obsidian. *The*
1295 *Canadian Mineralogist* **45**, 551–557.
- 1296 Manceau A. and Nagy K. L. (2012) Quantitative analysis of sulfur functional groups in natural
1297 organic matter by XANES spectroscopy. *Geochimica et Cosmochimica Acta* **99**, 206–
1298 223.
- 1299 Masotta M. and Keppler H. (2015) Anhydrite solubility in differentiated arc magmas.
1300 *Geochimica et Cosmochimica Acta* **158**, 79–102.
- 1301 Matjuschkin V., Blundy J. D. and Brooker R. A. (2016) The effect of pressure on sulphur
1302 speciation in mid-to deep-crustal arc magmas and implications for the formation of
1303 porphyry copper deposits. *Contributions to Mineralogy and Petrology* **171**, 66.
- 1304 McCanta M. C., Dyar M. D., Lanzirotti A., Newville M. and Breitenfeld L. B. (2019) In-situ
1305 mapping of ferric iron variations in lunar glasses using X-ray absorption spectroscopy.
1306 *American Mineralogist* **104**, 453–458.
- 1307 McCanta M. C., Dyar M. D., Rutherford M. J., Lanzirotti A., Sutton S. R. and Thomson B. J.
1308 (2017) In situ measurement of ferric iron in lunar glass beads using Fe-XAS. *Icarus* **285**,
1309 95–102.
- 1310 Métrich N., Berry A. J., O’Neill H. S. C. and Susini J. (2009) The oxidation state of sulfur in
1311 synthetic and natural glasses determined by X-ray absorption spectroscopy. *Geochimica*
1312 *et Cosmochimica Acta* **73**, 2382–2399.
- 1313 Métrich N., Bonnin-Mosbah M., Susini J., Menez B. and Galois L. (2002) Presence of sulfite
1314 (SIV) in arc magmas: Implications for volcanic sulfur emissions. *Geophysical Research*
1315 *Letters* **29**, 33-1-33–4.

- 1316 Métrich N. and Wallace P. J. (2008) Volatile abundances in basaltic magmas and their degassing
1317 paths tracked by melt inclusions. *Reviews in Mineralogy and Geochemistry* **69**, 363–402.
- 1318 de Moor J. M., Fischer T. P., Sharp Z. D., King P. L., Wilke M., Botcharnikov R. E., Cottrell E.,
1319 Zelenski M., Marty B., Klimm K., Rivard C. and Ayalew D. (2013) Sulfur degassing at
1320 Erta Ale (Ethiopia) and Masaya (Nicaragua) volcanoes: Implications for degassing
1321 processes and oxygen fugacities of basaltic systems. *Geochemistry, Geophysics,*
1322 *Geosystems* **14**, 4076–4108.
- 1323 Moussallam Y., Edmonds M., Scaillet B., Peters N., Gennaro E., Sides I. and Oppenheimer C.
1324 (2016) The impact of degassing on the oxidation state of basaltic magmas: A case study
1325 of Kīlauea volcano. *Earth and Planetary Science Letters* **450**, 317–325.
- 1326 Moussallam Y., Longpré M.-A., McCammon C., Gomez-Ulla A., Rose-Koga E. F., Scaillet B.,
1327 Peters N., Gennaro E., Paris R. and Oppenheimer C. (2019) Mantle plumes are oxidised.
1328 *Earth and Planetary Science Letters* **527**, 115798.
- 1329 Moussallam Y., Oppenheimer C., Scaillet B., Gaillard F., Kyle P., Peters N., Hartley M., Berlo
1330 K. and Donovan A. (2014) Tracking the changing oxidation state of Erebus magmas,
1331 from mantle to surface, driven by magma ascent and degassing. *Earth and Planetary*
1332 *Science Letters* **393**, 200–209.
- 1333 Muth M. J. and Wallace P. J. (2021) Slab-derived sulfate generates oxidized basaltic magmas in
1334 the southern Cascade arc (California, USA). *Geology*.
- 1335 Myers M. L. (2017) Storage, ascent, and release of silicic magma in caldera-forming eruptions.
1336 PhD Thesis, University of Oregon.
- 1337 Myers M. L., Wallace P. J., Wilson C. J., Morter B. K. and Swallow E. J. (2016) Prolonged
1338 ascent and episodic venting of discrete magma batches at the onset of the Huckleberry
1339 Ridge supereruption, Yellowstone. *Earth and Planetary Science Letters* **451**, 285–297.
- 1340 Nash W. M., Smythe D. J. and Wood B. J. (2019) Compositional and temperature effects on
1341 sulfur speciation and solubility in silicate melts. *Earth and Planetary Science Letters* **507**,
1342 187–198.
- 1343 Newville M. (2013) Larch: An analysis package for XAFS and related spectroscopies. In *Journal*
1344 *of Physics: Conference Series* IOP Publishing. p. 012007.
- 1345 O’Neill H. S. C., Berry A. J. and Mallmann G. (2018) The oxidation state of iron in Mid-Ocean
1346 Ridge Basaltic (MORB) glasses: Implications for their petrogenesis and oxygen
1347 fugacities. *Earth and Planetary Science Letters* **504**, 152–162.
- 1348 Osborn E. F. (1959) Role of oxygen pressure in the crystallization and differentiation of basaltic
1349 magma. *Am J Sci* **257**, 609–647.
- 1350 Papike J. J., Simon S. B., Burger P. V., Bell A. S., Shearer C. K. and Karner J. M. (2016)
1351 Chromium, vanadium, and titanium valence systematics in Solar System pyroxene as a

- 1352 recorder of oxygen fugacity, planetary provenance, and processes. *American*
1353 *Mineralogist* **101**, 907–918.
- 1354 Paris E., Giuli G., Carroll M. R. and Davoli I. (2001) The valence and speciation of sulfur in
1355 glasses by X-ray absorption spectroscopy. *The Canadian Mineralogist* **39**, 331–339.
- 1356 Ravel B. and Newville M. (2005) ATHENA, ARTEMIS, HEPHAESTUS: data analysis for X-
1357 ray absorption spectroscopy using IFEFFIT. *Journal of synchrotron radiation* **12**, 537–
1358 541.
- 1359 Righter K., Danielson L. R., Pando K., Morris R. V., Graff T. G., Agresti D. G., Martin A. M.,
1360 Sutton S. R., Newville M. and Lanzirotti A. (2013) Redox systematics of martian
1361 magmas with implications for magnetite stability. *American Mineralogist* **98**, 616–628.
- 1362 Rose T. and Brown C. (2017) Status of the Smithsonian Microbeam Standards 2017 With a
1363 Discussion of the Venerable VG-2 Basalt Glass. *Microscopy and Microanalysis* **23**, 498–
1364 499.
- 1365 Rose-Koga E. F., Bouvier A.-S., Gaetani G. A., Wallace P. J., Allison C. M., Andrys J. A., de la
1366 Torre CA A., Barth A., Bodnar R. J., Ajj B. G., Butters, Castillejo A., Chilson-Parks B.,
1367 Choudhary B. R., Cluzel N., Cole M., Cottrell E., Daly A., Danyushevsky L. V., Cl D.,
1368 Drignon M. J., France L., Gaborieau M., Garcia M. O., Gatti E., Genske F. S., Hartley,
1369 Hughes E. C., Iveson A. A., Johnson E. R., Jones M., Kagoshima T., Katzir Y.,
1370 Kawaguchi M., Kawamoto T., Kelley K. A., Koornneef J. M., Kurz, Laubier M., Layne
1371 G. D., Lerner A., Lin K.-Y., Liu P.-P., Lorenzo-Merino A., Luciani N., Magalhães N.,
1372 Marschall H. R., Michael P. J., Monteleone B. D., Moore L. R., Moussallam Y., Muth
1373 M., Myers M. L., Narváez D. F., Navon O., Newcombe, Arl N., Nielsen R. L., Pamukcu
1374 A., Plank T., Rasmussen D. J., Roberge J., Schiavi F., Schwartz, Kei S., Shimizu K.,
1375 Shimizu N., Thomas J. B., Thompson G. T., Tucker J. M., Ustunisik G., Waelkens C.,
1376 Zhang Y. and Zhou T. (2021) Silicate melt inclusions in the new millennium: A review
1377 of recommended practices for preparation, analysis, and data presentation. *Chemical*
1378 *Geology*, 120145.
- 1379 Rowe M. C., Kent A. J. and Nielsen R. L. (2007) Determination of sulfur speciation and
1380 oxidation state of olivine hosted melt inclusions. *Chemical Geology* **236**, 303–322.
- 1381 Schreiber H. D., Merkel Jr R. C., Schreiber V. L. and Balazs G. B. (1987) Mutual interactions of
1382 redox couples via electron exchange in silicate melts: models for geochemical melt
1383 systems. *Journal of Geophysical Research: Solid Earth* **92**, 9233–9245.
- 1384 Sharp T. G., Stevenson R. J. and Dingwell D. B. (1996) Microlites and “nanolites” in rhyolitic
1385 glass: microstructural and chemical characterization. *Bull Volcanol* **57**, 631–640.
- 1386 Shorttle O., Moussallam Y., Hartley M. E., Maclennan J., Edmonds M. and Murton B. J. (2015)
1387 Fe-XANES analyses of Reykjanes Ridge basalts: Implications for oceanic crust’s role in
1388 the solid Earth oxygen cycle. *Earth and Planetary Science Letters* **427**, 272–285.

- 1389 Sutton S. R., Lanzirotti A., Newville M., Dyar M. D. and Delaney J. (2020) Oxybarometry and
1390 valence quantification based on microscale X-ray absorption fine structure (XAFS)
1391 spectroscopy of multivalent elements. *Chemical Geology* **531**, 119305.
- 1392 Sutton S. R., Lanzirotti A., Newville M., Rivers M. L., Eng P. and Lefticariu L. (2017) Spatially
1393 resolved elemental analysis, spectroscopy and diffraction at the GSECARS Sector at the
1394 Advanced Photon Source. *Journal of environmental quality* **46**, 1158–1165.
- 1395 Tassara S., Reich M., Cannatelli C., Konecke B. A., Kausel D., Morata D., Barra F., Simon A.
1396 C., Fiege A. and Morgado E. (2020) Post-melting oxidation of highly primitive basalts
1397 from the southern Andes. *Geochimica et Cosmochimica Acta* **273**, 291–312.
- 1398 Tuffen H., Flude S., Berlo K., Wadsworth F. and Castro J. (2021) Obsidian. In *Encyclopedia of*
1399 *Geology (Second Edition)* (eds. D. Alderton and S. A. Elias). Academic Press, Oxford.
1400 pp. 196–208.
- 1401 Wallace P. J., Anderson Jr A. T. and Davis A. M. (1999) Gradients in H₂O, CO₂, and exsolved
1402 gas in a large-volume silicic magma system: Interpreting the record preserved in melt
1403 inclusions from the Bishop Tuff. *Journal of Geophysical Research: Solid Earth* **104**,
1404 20097–20122.
- 1405 Wallace P. J. and Carmichael I. S. E. (1994) S speciation in submarine basaltic glasses as
1406 determined by measurements of SK α X-ray wavelength shifts. *American Mineralogist*
1407 **79**, 161–167.
- 1408 Wallace P. J., Dufek J., Anderson A. T. and Zhang Y. (2003) Cooling rates of Plinian-fall and
1409 pyroclastic-flow deposits in the Bishop Tuff: inferences from water speciation in quartz-
1410 hosted glass inclusions. *Bulletin of Volcanology* **65**, 105–123.
- 1411 Wallace P. J., Plank T., Bodnar R. J., Gaetani G. A. and Shea T. (2021) Olivine-Hosted Melt
1412 Inclusions: A Microscopic Perspective on a Complex Magmatic World. *Annual Review of*
1413 *Earth and Planetary Sciences* **49**.
- 1414 Watkins J. M., Gardner J. E. and Befus K. S. (2017) Nonequilibrium degassing, regassing, and
1415 vapor fluxing in magmatic feeder systems. *Geology* **45**, 183–186.
- 1416 Waychunas G. A., Apter M. J. and Brown G. E. (1983) X-ray K-edge absorption spectra of Fe
1417 minerals and model compounds: Near-edge structure. *Phys Chem Minerals* **10**, 1–9.
- 1418 Weaver S. L., Wallace P. J. and Johnston A. D. (2011) A comparative study of continental vs.
1419 intraoceanic arc mantle melting: Experimentally determined phase relations of hydrous
1420 primitive melts. *Earth and Planetary Science Letters* **308**, 97–106.
- 1421 Wilke M., Farges F., Partzsch G. M., Schmidt C. and Behrens H. (2007) Speciation of Fe in
1422 silicate glasses and melts by in-situ XANES spectroscopy. *American Mineralogist* **92**,
1423 44–56.

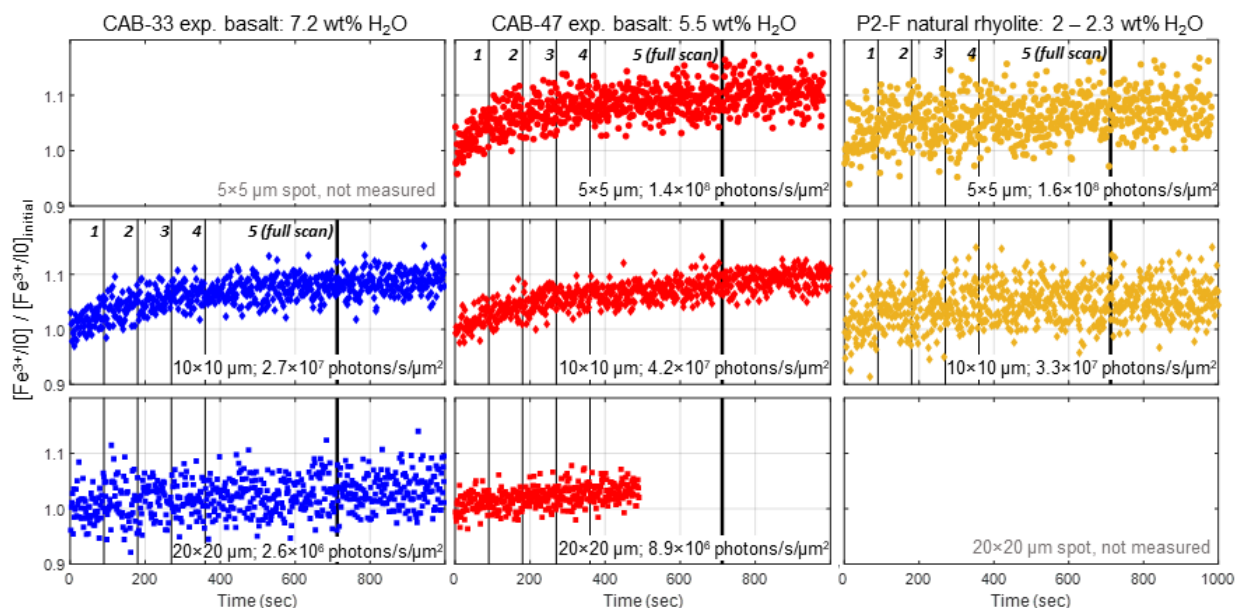
- 1424 Wilke M., Farges F., Petit P.-E., Brown Jr G. E. and Martin F. (2001) Oxidation state and
1425 coordination of Fe in minerals: An Fe K-XANES spectroscopic study. *American*
1426 *Mineralogist* **86**, 714–730.
- 1427 Wilke M., Jugo P. J., Klimm K., Susini J., Botcharnikov R., Kohn S. C. and Janousch M. (2008)
1428 The origin of S⁴⁺ detected in silicate glasses by XANES. *American Mineralogist* **93**, 235–
1429 240.
- 1430 Wilke M., Klimm K. and Kohn S. C. (2011) Spectroscopic studies on sulfur speciation in
1431 synthetic and natural glasses. *Reviews in Mineralogy and Geochemistry* **73**, 41–78.
- 1432 Wilke M., Partzsch G. M., Bernhardt R. and Lattard D. (2004) Determination of the iron
1433 oxidation state in basaltic glasses using XANES at the K-edge. *Chemical Geology* **213**,
1434 71–87.
- 1435 Wilke M., Schmidt C., Farges F., Malavergne V., Gautron L., Simionovici A., Hahn M. and Petit
1436 P.-E. (2006) Structural environment of iron in hydrous aluminosilicate glass and melt-
1437 evidence from X-ray absorption spectroscopy. *Chemical Geology* **229**, 144–161.
- 1438 Zhang H. L., Cottrell E., Solheid P. A., Kelley K. A. and Hirschmann M. M. (2018)
1439 Determination of Fe³⁺/ΣFe of XANES basaltic glass standards by Mössbauer
1440 spectroscopy and its application to the oxidation state of iron in MORB. *Chemical*
1441 *Geology* **479**, 166–175.
- 1442 Zhang H. L., Hirschmann M. M., Cottrell E., Newville M. and Lanzirotti A. (2016) Structural
1443 environment of iron and accurate determination of Fe³⁺/ΣFe ratios in andesitic glasses by
1444 XANES and Mössbauer spectroscopy. *Chemical Geology* **428**, 48–58.
- 1445
- 1446

1447 **Appendix A. Supplemental text and figures**

1448

1449 **Fe-XANES beam damage assessment and corrections, additional figures**

1450

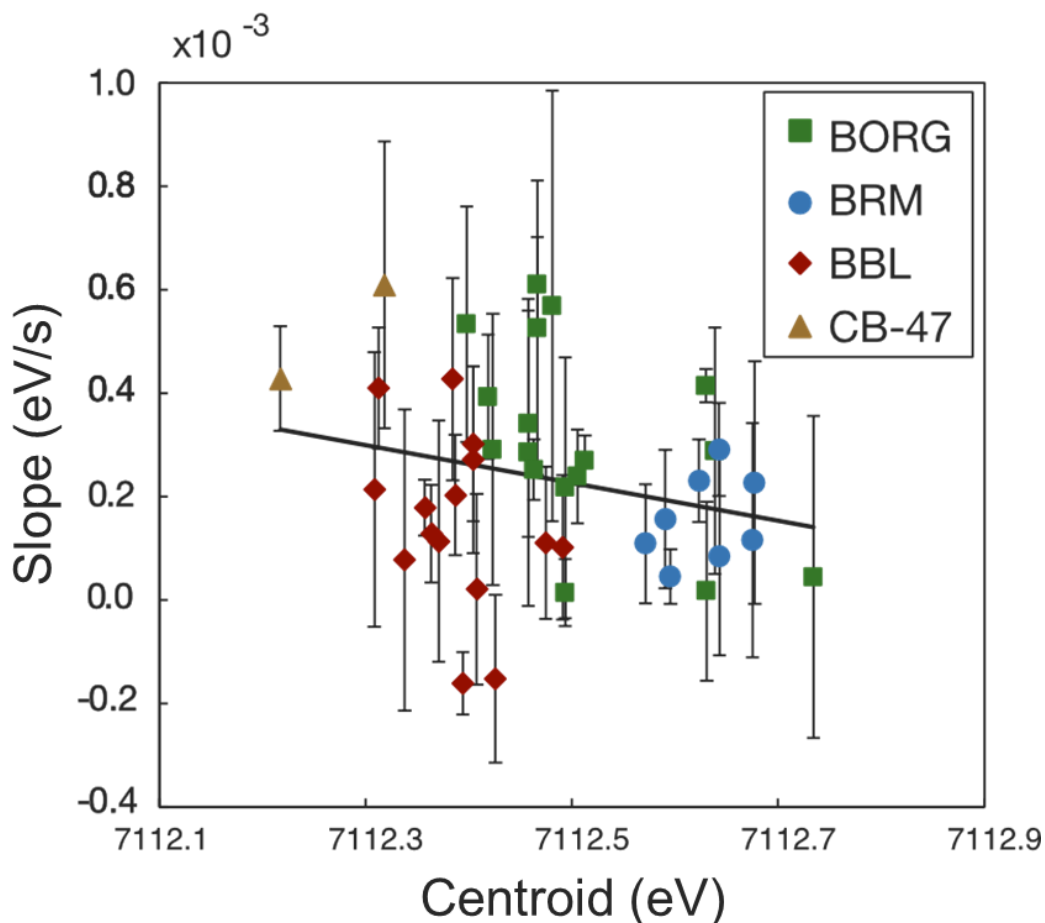


1451

1452 **Figure A.1.** Time dependence of the relative increase of 2nd pre-edge doublet ($[Fe-K\alpha/I_0] / [Fe$
 1453 $K\alpha/I_{0_{initial}}]$ at ~ 7113.4 eV, which we consider to be $Fe^{3+}/Fe^{3+_{initial}}$) during irradiation with X-ray
 1454 beams of $5 \times 5 \mu m$ (*upper*), $10 \times 10 \mu m$ (*middle*), and $20 \times 20 \mu m$ (*lower*) footprint sizes. $Fe^{3+_{initial}}$ is
 1455 the average of the first 10 measurements (13 – 15 s of analysis). Thin vertical lines (labeled 1 –
 1456 4) indicate analysis end times for repeat pre-edge Fe-XANES analyses (0.5 s/point), as described
 1457 in the text. The thick vertical line (labeled 5 full scan) is the end time after the final full energy
 1458 scan. Beam damage occurs rapidly in analyses with a focused $5 \times 5 \mu m$ beam. However, linear
 1459 time-dependent functions can be regressed through the rapid scanning sequence in the first 4.5 –
 1460 6 minutes of analyses with 10×10 and $20 \times 20 \mu m$ beams to correct beam-damaged induce
 1461 oxidation to the initial ($t=0$ s) conditions. Photon flux densities for analyses with 5×5 , 10×10 ,
 1462 and $20 \times 20 \mu m$ beams were $1.4 - 1.6 \times 10^8$, $2.7 - 4.2 \times 10^7$, and $2.6 - 8.9 \times 10^6$ photons/s/ μm^2 ,
 1463 respectively. We note that experimental glass CAB-33 has a spectral signature that suggests with
 1464 the presence of Fe-oxide nanolites (see section 3.1; **Data supplement**).

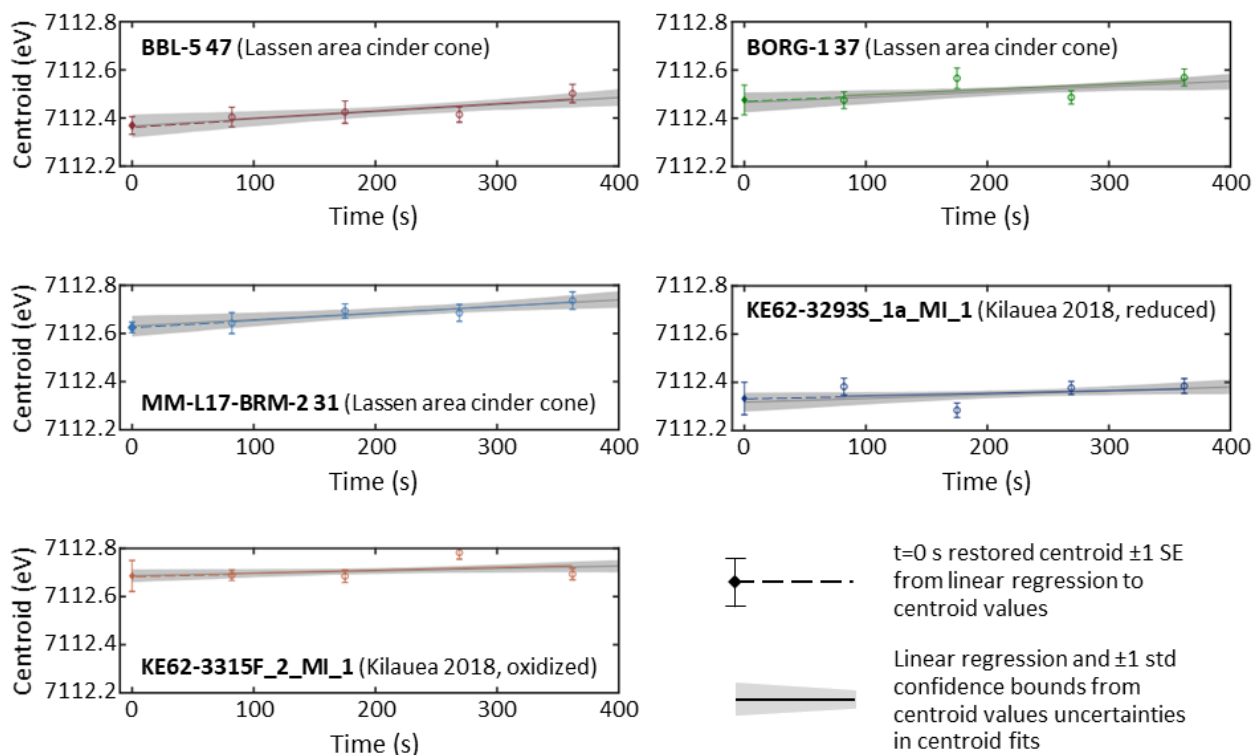
1465

1466



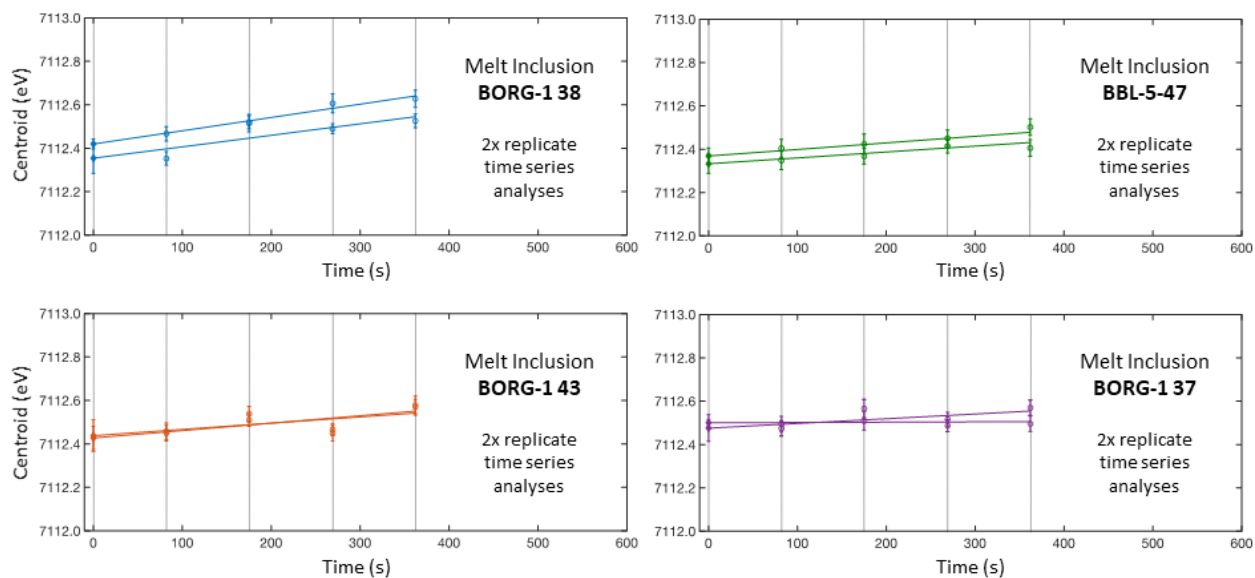
1467
 1468 **Figure A.2.** Slopes of linear regressions through Fe- $K\alpha$ pre-edge centroid time series as a
 1469 function of the centroid position of the first rapid scan (least affected by beam damage) for
 1470 individual samples. The slope of each centroid linear regression can be used as a proxy for the
 1471 rate of photo-oxidation. The values of these slopes show an inverse correlation with calculated
 1472 initial $\text{Fe}^{3+}/\Sigma\text{Fe}$ and a positive correlation with H_2O content of each glass (Figure 5), indicating
 1473 that beam damage occurs more readily in reduced and/or hydrous glasses (Cottrell et al., 2018).
 1474 Although the estimated initial $\text{Fe}^{3+}/\Sigma\text{Fe}$ is itself dependent on the slope of each regression, the
 1475 observed correlation between slope values and $\text{Fe}^{3+}/\Sigma\text{Fe}$ is not simply an artifact; this plot shows
 1476 that the centroid values of the first, least beam-damaged pre-edge scan of each analysis spot
 1477 shares the same correlation between $t=0$ regression slopes and calculated $\text{Fe}^{3+}/\Sigma\text{Fe}$. Melt
 1478 inclusions from three cinder cones in the southern Cascade arc (BORG, BRM, BBL) and
 1479 experimental glasses (CAB-47) are grouped by color. Gray line represents linear fit through all
 1480 data. All centroids have been shifted by +0.32 eV for consistency with the LW_0 centroid
 1481 position reported by Cottrell et al. (2009). See section 2.2 for further discussion.
 1482

1483



1484

1485 **Figure A.3.** Fe- $K\alpha$ pre-edge centroid positions calculated from repeated rapid scans of natural
 1486 melt inclusions shown in Figure 4. Circles represent the centroid values calculated from one pre-
 1487 edge scan. Error bars represent ± 1 SE for individual centroid fits. Colored lines are linear
 1488 regressions through measured centroid values from 82 to 362 s. Diamonds at $t=0$ s are the
 1489 intercept of each linear regression to the centroid time series, and are taken to be the beam
 1490 damage-corrected initial centroid position. Error bars on corrected initial centroid positions
 1491 represent ± 1 SE of the time series linear regression. Gray bands show ± 1 standard deviation non-
 1492 simultaneous prediction bounds for the linear fit function calculated using a Monte Carlo
 1493 approach as described in main text. Note that the $t=0$ s regressions for the H_2O -poor Kīlauea melt
 1494 inclusions are essentially flat, in contrast to the $t=0$ s regressions for the more hydrous (and beam
 1495 damage susceptible) subduction zone melt inclusions from the Lassen area cinder cones.
 1496



1497

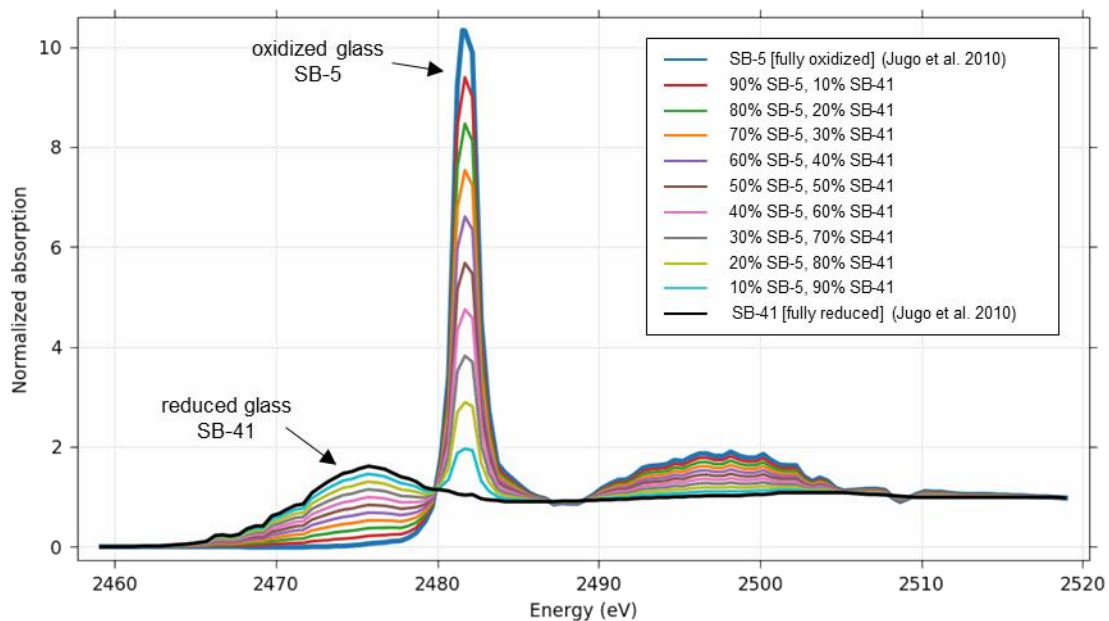
1498 **Figure A.4.** Centroid positions calculated from replicate sets of rapid pre-edge Fe-XANES scans
 1499 within single melt inclusions from the southern Cascades. Analyses were conducted with a
 1500 $10 \times 10 \mu\text{m}$ beam and photon flux densities of $3 - 5 \times 10^7$ photons/s/ μm^2 . Each sequence represents
 1501 repeated measurements in one analyzed spot. Open circles are centroids calculated for each pre-
 1502 edge scan. Error bars represent ± 1 SE of centroid fits to individual scans. Filled diamonds at t=0
 1503 s are the intercept of each linear regression and are used as the time-corrected initial centroid
 1504 values. Error bars on the t=0 s centroids represent ± 1 SE of each time series linear regression.
 1505 Vertical lines indicate analysis end times for repeat pre-edge Fe-XANES analyses. All centroids
 1506 have been shifted by +0.32 eV for consistency with the LW_0 centroid position reported by
 1507 Cottrell et al. (2009).
 1508

1509 **S-XANES peak fitting details**

1510 Our S-XANES peak fitting approach is calibrated to the suite of experimental hydrous
1511 basaltic glasses (45 – 48 wt% SiO₂, 8 – 10 wt% FeO^T, 8 – 10 wt% CaO, 200 MPa, 1050 °C)
1512 presented in Jugo et al. (2010) (see **Data supplement**). These glasses were synthesized at
1513 different oxidation states and were used by Jugo et al. (2010) to develop an empirical fit
1514 relationship of S²⁻ and S⁶⁺ S-XANES intensities to sulfur speciation. The Jugo et al. (2010)
1515 calibration was based on the assumption that sulfur in their most reduced and oxidized end-
1516 member glasses occurred entirely as S²⁻ and S⁶⁺, respectively, and that linear combination fitting
1517 of the end-members produces representative spectra for glasses with mixed sulfur speciation.
1518 Using these end-members and linear combination mixed spectra, Jugo et al. (2010) constructed a
1519 calibration of S-XANES intensity to sulfur speciation across a range of mixed sulfur states
1520 (Figure A.5). We note that the presumed linear combination relationship between end-member
1521 sulfur-intensities and sulfur speciation has not been shown independently to be true, but in
1522 absence of confirmation from Mössbauer or wet chemistry measurements, it is currently a
1523 reasonable assumption and the results agree well with thermodynamic calculations (Jugo et al.,
1524 2010).

1525 We use S-XANES spectra for the end-member reduced and oxidized glasses presented in
1526 Jugo et al. (2010) to construct linear mixtures of the two and create a S-XANES intensity to
1527 sulfur speciation calibration for our peak fitting method (see section 2.3 for details). The main
1528 difference between our peak fitting method and the Jugo method is that we isolate the S⁶⁺ peak
1529 from the slightly higher energy ionization peak. By including the ionization peak in our fit
1530 procedure, we end up with no S⁶⁺ intensity in S⁶⁺-free glasses, whereas the Jugo et al. (2010) fit
1531 method either convolutes the S⁶⁺ peak with the ionization peak or fits the step-function
1532 background differently than we do, which results in ~0.3 I[S⁶⁺]/IΣS XANES intensity present in
1533 S⁶⁺-free glasses. Applying our peak fitting to the full set of hydrous experimental glasses (200
1534 MPa, 1050 °C, FMQ -1.4 to +2.7) presented in Jugo et al. (2010), we find good agreement
1535 between sulfur speciation calculated from our method with that of Jugo et al. (2010) (Figure A.8;
1536 see **Data supplement**).

1537



1538

1539 **Figure A.5.** Normalized spectra of completely oxidized (SB-5; FMQ +2.7; $S^{6+}/S\Sigma = 1.00$; blue
 1540 curve) and completely reduced (SB-41; FMQ -1.4; $S^{6+}/S\Sigma = 0.00$, black curve) hydrous
 1541 experimental glasses reproduced from Jugo et al. (2010) (see **Data supplement**). Linear two-
 1542 component mixing of these endmember glasses provides a simulated set of spectra to calibrate S-
 1543 XANES intensities to sulfur speciation in glasses in both Jugo et al. (2010) and in the peak-
 1544 fitting method presented here. An energy shift of -1 eV has been applied to all the Jugo et al.
 1545 (2010) data (see section 2.3.1).

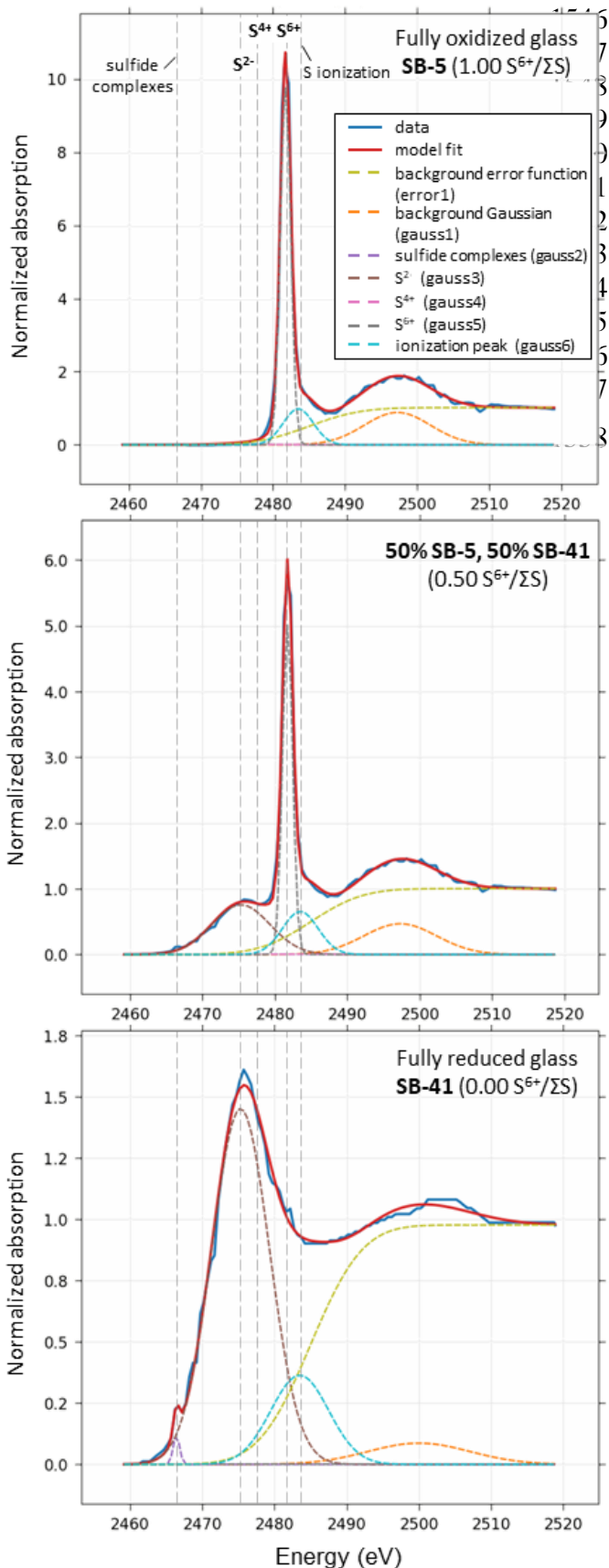
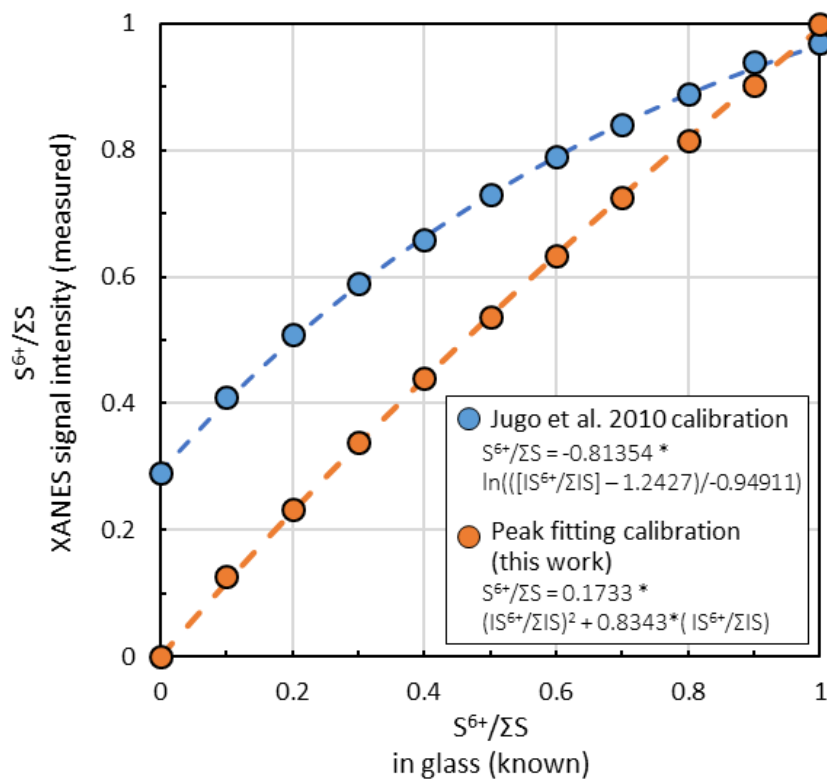
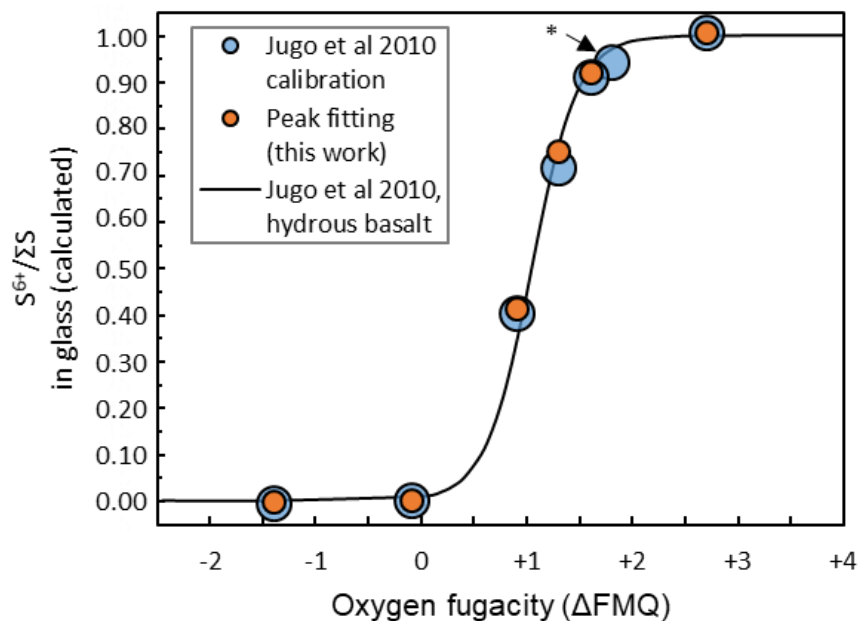


Figure A.6. Example peak fits to the normalized end-member oxidized (*upper*) and reduced (*lower*) hydrous experimental glasses reproduced from Jugo et al. (2010), as well as a 50% linear mixture of the two endmembers (*middle*). Parameters of the fit functions are identified in Table 2. Reference peak position lines may vary slightly between samples. An energy shift of -1 eV has been applied to all the Jugo et al. (2010) data (see section 2.3.1).



1559
 1560 **Figure A.7.** Fit relationships between S-XANES S⁶⁺/ΣS signal intensity and S⁶⁺/ΣS speciation in
 1561 experimental end-member hydrous glasses and linear component mixtures for the Jugo et al.
 1562 (2010) calibration (blue) and the peak fitting calibration in this study (orange). Relative
 1563 uncertainties in S⁶⁺/ΣS signal intensities from S-XANES peak fitting are estimated to be ±7%
 1564 (2RSE) based on the reproducibility of spectral fitting (see **Data supplement**).
 1565



1566

1567 **Figure A.8.** Calculated sulfur speciation vs $f\text{O}_2$ experimental conditions of the set of synthesized
 1568 hydrous glasses from Jugo et al. (2010), with XANES spectral fits from our peak fitting method
 1569 (orange) compared to the Jugo et al. (2010) approach (blue) (see **Data supplement**). Only the
 1570 most oxidized and reduced glasses were used to calibrate the peak fitting method. Applying our
 1571 peak fitting method to the Jugo et al. (2010) suite of glass samples synthesized at intermediate
 1572 $f\text{O}_2$ shows that the two methods calculate very similar $S^{6+}/\Sigma S$ values. Relative uncertainty in
 1573 $S^{6+}/\Sigma S$ calculations via the peak fitting method is estimated to be $\pm 10\%$ based on the
 1574 reproducibility of spectra normalization and fitting. The “*” symbol indicates that the normalized
 1575 XANES spectrum for this glass was not presented in Jugo et al. (2010), precluding inclusion in
 1576 our comparison. The black curve is the Jugo et al. (2010) predicted relation of $f\text{O}_2$ and $S^{6+}/\Sigma S$ for
 1577 a hydrous basalt at 1050°C and 200 MPa.

1578

1579

1580 **Appendix References**

- 1581 Cottrell E., Kelley K. A., Lanzirotti A. and Fischer R. A. (2009) High-precision determination of
1582 iron oxidation state in silicate glasses using XANES. *Chemical Geology* **268**, 167–179.
- 1583 Cottrell E., Lanzirotti A., Mysen B., Birner S., Kelley K. A., Botcharnikov R., Davis F. A. and
1584 Newville M. (2018) A Mössbauer-based XANES calibration for hydrous basalt glasses
1585 reveals radiation-induced oxidation of Fe. *American Mineralogist* **103**, 489–501.
- 1586 Jugo P. J., Wilke M. and Botcharnikov R. E. (2010) Sulfur K-edge XANES analysis of natural
1587 and synthetic basaltic glasses: Implications for S speciation and S content as function of
1588 oxygen fugacity. *Geochimica et Cosmochimica Acta* **74**, 5926–5938.